J. Fluid Mech. (1998), *vol.* 376, *pp.* 149–182. Printed in the United Kingdom

A numerical study of the sedimentation of fibre suspensions

By MICHAEL B. MACKAPLOW† AND ERIC S. G. SHAQFEH
Department of Chemical Engineering, Stanford University, Stanford, CA 94305-5025, USA

(Received 15 April 1997 and in revised form 26 May 1998)

The sedimentation of fibre suspensions at low Reynolds number is studied using two different, but complementary, numerical simulation methods: (1) Monte Carlo simulations, which consider interparticle hydrodynamic interactions at all orders within the slender-body theory approximation (Mackaplow & Shaqfeh 1996), and (ii) dynamic simulations, which consider point–particle interactions and are accurate for suspension concentrations of $nl^3 \gg 1$, where n and l are the number density and characteristic half-length of the fibres, respectively. For homogeneous, isotropic suspensions, the Monte Carlo simulations show that the hindrance of the mean sedimentation speed is linear in particle concentration up to at least $nl^3 = 7$. The speed is well predicted by a new dilute theory that includes the effect of two-body interactions. Our dynamic simulations of dilute suspensions, however, show that interfibre hydrodynamic interactions cause the spatial and orientational distributions to become inhomogeneous and anisotropic. Most of the fibres migrate into narrow *streamers* aligned in the direction of gravity. This drives a downward convective flow within the streamers which serves to increase the mean fibre sedimentation speed. A steady-state orientation distribution develops which strongly favours fibre alignment with gravity. Although the distribution reaches a steady state, individual fibres continue to rotate in a manner that can be qualitatively described as a *flipping* between the two orientations aligned with gravity. The simulation results are in good agreement with published experimental data.

1. Introduction

Sedimenting suspensions exist in many natural and man-made systems. Examples include the movement of pollution in the atmosphere (e.g. acid rain), clarification of wastewater, and the production of fibre composites. Additionally, analysis of the sedimentation behaviour of red blood cells (ESR) is used as a diagnostic medical tool (Reinhart, Singh & Werner 1989). However, despite the universality of particle sedimentation, there are still many unanswered fundamental questions regarding it.

The mobilities of isolated sedimenting particles can be determined theoretically or experimentally. However, even at relatively low concentrations, the effect of particle interactions on the sedimentation speed becomes significant. For example, in a fluid containing a 3% volume fraction of spheres, the interparticle hydrodynamic interactions reduce the mean sphere sedimentation speed nearly 20% (Batchelor 1972); for elongated bodies, interactions become important at even lower concentrations

† Present address: PPD Process Development Center, Abbott Laboratories, Dept. 4P8, Bldg. R1B, 1401 Sheridan Road, North Chicago, IL 60064-4000, USA.

(Turney *et al.* 1995). These strong effects occur because the influence of one sedimenting particle on the velocity of another decays slowly, as $1/r$ (Batchelor 1972; Ladd 1990), where r is the distance between the two bodies. Even for a given concentration, a suspension's sedimentation behaviour will strongly depend on the particle centre-of-mass distribution. This distribution is generally not known. It is simplest to assume the suspension is homogeneous throughout the settling process (Batchelor 1972). Theoretical studies have suggested this is a good assumption for spheres, but not for fibres (Koch & Shaqfeh 1989).

For our subsequent discussion and later numerical analysis, we restrict ourselves to sedimenting, periodic suspensions meeting the following set of conditions: (i) both the particle and fluid Reynolds numbers are much less than unity, so inertia can be neglected; (ii) the particle Péclet number is much greater than unity, so Brownian forces can be neglected; (iii) the only external body force acting on the particles is gravity; (iv) the only interparticle interactions are hydrodynamic (e.g. no electrostatic forces).

Because they are isotropic bodies, sedimenting suspensions of spheres are the simplest system to study. Much early experimental work focused on developing correlations for the mean sedimentation speed of monodisperse sphere suspensions as a function of concentration. Such investigations predicted the form of the hindrance function, $f(\phi)$, defined by $\langle U\rangle/U_{sphere} \equiv f(\phi)$, where $\langle U\rangle$ is the mean sphere sedimentation speed, U_{sphere} is the sedimentation speed of an isolated sphere, and ϕ is the volume fraction of spheres in the suspension (Richardson & Zaki 1954; Barnea & Mizrahi 1973). Early theoretical attempts to take into account interparticle interactions, and thus predict $f(\phi)$ *a priori*, used cell models (Barnea & Mizrahi 1973). All such models predict hindrance functions of the form

$$f(\phi)\ 1-O(\phi^{1/3}) \tag{1.1}$$

which is the same form as that for a dilute periodic array of spheres (Hasimoto 1959). In contrast, Batchelor (1972) explicitly considered the effect of two-body interactions on the mean sedimentation speed in a dilute suspension of spheres. By assuming that the sedimenting suspension was random and homogeneous, he determined that

$$f(\phi) = 1-6.55\phi+O(\phi^2) \tag{1.2}$$

for ϕ 1. Equation (1.2) shows that for ϕ 1 the effect of interparticle interactions is much less in disordered suspensions than that predicted by cell models. Since this early work, there have been many further experimental, theoretical, and numerical studies of sedimenting suspensions of spheres. A review article by Davis & Acrivos (1985) summarizes many of the discoveries. Some discussion of developments following the aforementioned review is given by Nicolai *et al.* (1995). Our purpose is not to give a detailed overview of scientific advances concerning the understanding of the sedimentation of suspensions of spheres. We wish to merely point out that there has been significant progress toward ultimately understanding this process.

On the other hand, the sedimentation behaviour of suspensions of fibres (or non-spherical particles in general) is much more complicated and has received much less attention. Insight into these additional complications can be gained by first examining the equation for the sedimentation velocity of a single, isolated prolate spheroid under Stokes' flow conditions (Oberbeck 1876; Happel & Brenner 1965)

$$\boldsymbol{U}_{spheroid} = \frac{V_p g\Delta\rho}{16\pi\eta_0 l}(\alpha_0\boldsymbol{\delta}+\alpha_1\boldsymbol{pp})\cdot\hat{\boldsymbol{g}}, \tag{1.3}$$

where A is spheroid aspect ratio,

$$\alpha_0 \equiv \frac{A^2}{A^2-1}+\frac{2A^3-3A}{(A^2-1)^{3/2}}\ln\left[A+(A^2-1)^{1/2}\right],$$

$$\alpha_1 \equiv \frac{-3A^2}{A^2-1}+\frac{2A}{(A^2-1)^{3/2}}\ln\left[A+(A^2-1)^{3/2}\right]+\frac{A-2A^3}{(A^2-1)^{3/2}}\ln\left[A-(A^2-1)^{1/2}\right],$$

$\Delta\rho$ is the density difference between the fibre and the surrounding fluid, V_P is the volume of the spheroid, g is the gravitational constant, $\hat{\boldsymbol{g}}$ is the unit vector in the direction of gravity, η_0 is fluid viscosity, l is the half-length of the long axis, and $\boldsymbol{p}$ is the spheroid orientation.

Clearly, the sedimentation speed is a function of the particle orientation relative to gravity. Since α_0 and α_1 are always positive, the speed is largest when the particle is aligned with gravity and slowest when perpendicular to it. The difference in the sedimentation speeds at the two extremes of orientation increases with particle aspect ratio. The variation of sedimentation speed with orientation is not limited to particles of spheroidal shape. In particular, for a fibre of any shape we can use slender-body theory as developed by Batchelor (1970) to show that the sedimentation velocity is given by

$$\boldsymbol{U}_{SED} = \frac{V_p g\Delta\rho}{8\pi\eta_0 l}\left[(\ln 2A + C_1 + O(\ln 2A)^{-1})\,\boldsymbol{\delta} + (\ln 2A + C_2 + O(\ln 2A)^{-1})\,\boldsymbol{pp}\right]\cdot\hat{\boldsymbol{g}}, \quad (1.4)$$

where C_1 and C_2 are $O(1)$ constants that are functions of the body shape. For prolate spheroids, $C_1 = 1/2$ and $C_2 = -3/2$. For cylinders, $C_1 = 0.193$ and $C_2 = -1.807$. The ratio of the maximum and minimum fall speeds asymptotically approaches 2 in the limit of infinite aspect ratio. The variation of fall speed with orientation is substantial even for moderate aspect ratio bodies. For example, there is more than a 40% variation for spheroids with an aspect ratio of 10. Since the effect of a sedimenting particle on the angular velocity of another particle is long-ranged, decaying as $1/r^2$ (Ladd 1990), this distribution is influenced by particle interactions. Indeed, the orientation distribution is indeterminate without knowledge of the hydrodynamic interactions.

The coupling between hydrodynamic interactions and orientation distributions is particularly interesting at dilute concentrations, defined as $nl^3 < O(1)$, where n is the fibre number density and l is the fibre half-length. At such concentrations, the instantaneous effect on the velocity of a given fibre by the other fibres is only $O(nl^3)$. However, since the interactions also cause particle rotations, they indirectly have an $O(1)$ effect on the velocity. Additionally, unlike spheres at such concentrations (Ham & Homsy 1988), the individual fibres will have substantial motion perpendicular to gravity. This 'drift velocity' depends strongly on fibre orientation and increases with aspect ratio. For spheroids with an aspect ratio of 10, it may be as high as 20% of the sedimentation speed. The fact that interfibre hydrodynamic interactions have an $O(1)$ effect on both the drift velocities and sedimentation speeds of individual bodies suggests that, compared to a sedimenting suspension of spheres, spatial inhomogeneities are more likely to form. In fact, inhomogeneities in sedimenting suspensions of non-Brownian fibres have recently been witnessed in the laboratory (Herzhaft *et al*. 1996) and we shall refer to these results throughout the present study.

Quite possibly due to the aforementioned complexities, there have been few

fundamental studies of fibre sedimentation. Kuwabara (1959) proposed a cell model to determine the sedimentation velocity of suspensions of fibres oriented perpendicular to gravity. However, since cell models fail to predict the proper scaling of the hindered settling function with concentration for spheres, as discussed earlier, it is not clear that they will be successful for suspensions of fibres. Koch & Shaqfeh (1989) studied the effect of two-particle interactions on the centre-of-mass pair probability distribution function in dilute suspensions. Their analysis shows that these interactions cause an increase in the density of particles around a sedimenting particle. Moreover, they completed a linear stability analysis showing that a homogeneous suspension of fibres, unlike a suspension of spheres, is unstable to density fluctuations. Their analysis also suggests that the sedimenting suspension should segregate into vertical *streamers*, regions of high particle density where hydrodynamic interactions cause a relatively strong downward convection of particles and fluid, and regions of low particle density where most of the fluid motion is opposite to the direction of gravity.

Claeys & Brady (1993*c*) used Stokesian Dynamics numerical simulations to study the sedimentation of periodic arrays of spheroids. These provide valuable information about hydrodynamic interactions in crystalline systems. However, for the reasons mentioned earlier, it is not clear that the scaling of sedimentation velocity with concentration in such systems will be the same as that in a disordered suspension. Additionally, they do not provide information about how hydrodynamic interactions affect the centre-of-mass and orientation distributions.

Experimental studies (Anselmet 1989; Kumar & Romarao 1991; Turney *et al.* 1995) have mainly focused on measuring the fall speed of the suspension interface, and assumed this to be the mean particle sedimentation speed. In sedimenting sphere suspensions, this interface is sharp (Davis & Acrivos 1985) and its fall speed approximates the mean particle sedimentation speed (Davis & Hassen 1988). In contrast, in a sedimenting fibre suspension, it is not sharp (Turney *et al.* 1995), nor is there any evidence that the fall rate of this 'interface', for any particular definition, is the same as the mean fibre sedimentation speed. Nonetheless, these experimental studies give us qualitative information about sedimenting fibre suspensions.

Turney *et al.* (1995) chose to examine the position of the interface where the fibre concentration was half that of the initial concentration. Their results showed the mean sedimentation speed decreasing with increasing concentration. Anselmet (1989) performed similar experiments. The two experimentally determined hindrance functions can be compared as a function of nl^3, since this is the relevant concentration for determining the extent of fibre interactions (Mackaplow, Shaqfeh & Schiek 1994; Mackaplow & Shaqfeh 1996). The results of Anselmet (1989) show a greater reduction in sedimentation speed as a function of nl^3 than those of Turney *et al.* (1995), although the discrepancy decreases with increasing concentration. As hypothesized by Turney *et al.* (1995), this discrepancy is consistent with the postulate that Anselmet (1989) used a sedimentation cell whose linear dimension in directions perpendicular to gravity was so small that the walls seriously affected the results. Similar experimental results were presented by Kumar & Ramarao (1993). Curiously, they found that the sedimentation speed dropped abruptly, and nearly vanished, at suspension volume fractions (independent of aspect ratio) greater than 0.015.

In contrast to previous experimental studies, Herzhaft *et al.* (1996) directly tracked the position and orientation of individual fibres in a dilute ($nl^3 < 1$) sedimenting suspension. The fibre orientation distribution evolves to strongly favour alignment with gravity. Individual fibres undergo flipping motions between the two orientations aligned with gravity. Fibre clustering was observed, which is qualitatively consistent

with the predictions of Koch & Shaqfeh (1989). This clustering created an increase in the mean sedimentation speed; an increase which was greater than that which could be accounted for by the change in the orientation distribution.

In summary, most existing experimental studies have estimated the mean sedimentation speed in a fibre suspension by the movement of the suspension/clear fluid interface. It is not known if this is a valid approximation. A more detailed study by Herzhaft *et al.* (1996), albeit at more dilute fibre concentrations, has yielded results that showed complicated physical behaviour, including suspension inhomogeneities. Existing theoretical work is qualitative and very limited, although it is in rough agreement with experimental results for non-dilute suspensions. Numerical methods have not been used to study disordered fibre suspensions.

We use numerical simulations to investigate the effect of hydrodynamic interactions on the sedimentation speed, orientation distribution, and positional configuration in an initially disordered sedimenting fibre suspension. Simulations have the advantage of allowing us to vary precisely the system parameters and examine more detailed transient data than is practically possible in an experimental system. In §2 we present Monte Carlo simulations. Fibres are represented as line distributions of Stokeslets in a periodic box. All fibre interactions are considered within the slender-body theory approximation. In isotropic suspensions, the hindrance of the mean particle sedimentation speed is linear in particle concentration at concentrations up to at least $nl^3 = 7$. The hindrance function is well predicted by the dilute theory corrected for the effects of two-body interactions, which is developed in Appendix C, and is in good agreement with the experimental results of Turney *et al.* (1995).

In §3 we present dynamic *point particle* simulations. In these simulations, each fibre is represented as point force whose mobility depends on its orientation. We verify the ability of these simulations to correctly capture fibre–fibre interactions at low concentrations by comparison with the aforementioned Monte Carlo simulations. The dynamic simulations predict that the orientation distribution in a dilute sedimenting suspension will evolve to favour orientations aligned with gravity. The suspension also becomes inhomogeneous, with most of the fibres migrating to form narrow *streamers* aligned in the direction of gravity. This agrees with the theoretical prediction of Koch & Shaqfeh (1989). As a result of this inhomogeneity, the mean sedimentation speed increases beyond that which can be attributed to the effect of the changing orientation distribution. Individual fibres undergo *flipping motions*, where a fibre spends most of its time in one of two orientations nearly aligned with gravity, while occasionally rapidly flipping between these two. The simulation results agree with the experimental work of Herzhaft *et al.* (1996).

2. Monte Carlo simulations

2.1. *Mathematical formulation of the problem and solution of the governing equations*

In this section we present the formulation and method of solution of the governing equations for our Monte Carlo simulations. This development is nearly identical to that used in our study of the rheological properties of fibre suspensions (Mackaplow & Shaqfeh 1996). Thus, only an overview of the development and the differences between the two formulations will be presented.

Consider an inertialess, monodisperse suspension of rigid, non-Brownian, fibres in a Newtonian fluid. The fibres have a length of $2l$, a characteristic width of $2b$, and a density that is $\Delta\rho$ greater than that of the surrounding fluid. Following Batchelor

(1970), slender-body theory can be used to represent the disturbance velocity created by a fibre, $\boldsymbol{v}^D(\boldsymbol{x})$, as an integral of Stokeslets, $\boldsymbol{F}(s)$ distributed along the fibre axis,

$$\boldsymbol{v}^D(\boldsymbol{x}) = \boldsymbol{v}(\boldsymbol{x}) - \boldsymbol{v}^\infty(\boldsymbol{x}) = \int \boldsymbol{F}(s)\cdot\boldsymbol{H}(\boldsymbol{x}-\boldsymbol{x}_c-s\boldsymbol{p})\,\mathrm{d}s\times(1+O(b/h)). \tag{2.1}$$

$\boldsymbol{H}(\boldsymbol{x})$ is the Oseen tensor, i.e. $(\boldsymbol{\delta}/|\boldsymbol{x}|+\boldsymbol{x}\boldsymbol{x}/|\boldsymbol{x}|^3)/8\pi\eta_0$, h is the distance of $\boldsymbol{x}$ from the major axis of the fibre, $\boldsymbol{v}^\infty(\boldsymbol{x})$ is the undisturbed velocity field, and $\boldsymbol{x}_c$ and $\boldsymbol{p}$ are the fibre centre position and orientation vector, respectively. $\boldsymbol{F}(\boldsymbol{s})$ can be related to the flow field experienced by a fibre using the method of matched asymptotic expansions (Batchelor 1970), namely

$$\begin{aligned}\boldsymbol{U}_j+\boldsymbol{\Omega}_j\times s\boldsymbol{p}_j = \boldsymbol{v}^\infty(\boldsymbol{x}_{c_j}+s\boldsymbol{p}_j)+\sum_{\substack{i=1\\ i\neq j}}^{N}\int \boldsymbol{H}(\boldsymbol{x}_{c_i}+s'\boldsymbol{p}_i-\boldsymbol{x}_{c_j}-s\boldsymbol{p}_j)\cdot\boldsymbol{F}_i(s')\,\mathrm{d}s'\\ +2\left(\ln 2A+\ln\frac{(1-s^2)^{1/2}}{\hat{b}(s)}\right)(\boldsymbol{\delta}+\boldsymbol{p}_j\boldsymbol{p}_j)\cdot\boldsymbol{F}_j(s)+(\boldsymbol{\delta}-3\boldsymbol{p}_j\boldsymbol{p}_j)\cdot\boldsymbol{F}_j(s)\\ +(\boldsymbol{\delta}+\boldsymbol{p}_j\boldsymbol{p}_j)\cdot\int\frac{\boldsymbol{F}_j(s)-\boldsymbol{F}_j(s')}{|s-s'|}\,\mathrm{d}s' \quad j=1,\ldots,N.\end{aligned} \tag{2.2}$$

The subscripts on $\boldsymbol{U}_j$, $\boldsymbol{\Omega}_j$, $\boldsymbol{p}_j$, $\boldsymbol{x}_{c_j}$, and $\boldsymbol{F}_j$ differentiate between fibres in the N-body system considered. The velocity of the fibre and its angular velocity about its centre are denoted by $\boldsymbol{U}$ and $\boldsymbol{\Omega}$, respectively, and $\hat{b}(s)$ is related to the local perimeter of the fibre cross-section, as discussed in detail by Batchelor (1970). The axial singularity distributions on each fibre must also satisfy

$$\left.\begin{aligned}\int\boldsymbol{F}_s(s)\,\mathrm{d}s &= \Delta\rho V_p\boldsymbol{g}, \qquad (2.3)\\ \left[\int s\boldsymbol{F}_j(s)\,\mathrm{d}s\right]\times\boldsymbol{p}_j &= 0, \qquad (2.4)\end{aligned}\right\} \quad j=1,\ldots,N.$$

The first equation states that each fibre exerts a force on the surrounding fluid equal to the gravitational body force that acts on it; the second states that no fibre is acted upon by an external torque. Combining (2.2), (2.3), and (2.4), yields a coupled set of integral equations. These equations can be non-dimensionalized using the characteristic fibre velocity and Stokeslet strength, $(|\boldsymbol{g}|V_p\Delta\rho)/(8\pi\eta_0 l)$ and $|\boldsymbol{g}|V_p\Delta\rho/l$, respectively, and then they can be solved to determine the velocity, angular velocity, and the strength of the singularity distribution on each fibre.

If we let h in equation (2.1) be the average interfibre spacing for a semidilute suspension, we find that the error introduced into the fibre interactions by the slender-body theory approximation is $O(\phi^{1/2})$. Thus, at suspension concentrations up through semidilute, the majority of fibre interactions are well approximated by the slender-body theory approximation. However, even at such concentrations, close hydrodynamic interactions occur that are not accounted for by slender-body theory. In particular, although we have omitted the details, it can be shown that when two fibres with dissimilar orientations have a closest approach within $O(b\ln A/A)$, the hydrodynamic lubrication force interaction alters the sedimentation speed of each fibre by an $O(1)$ amount. However, the probability that any given fibre in a semidilute suspensions will experience such an interaction is only $O(\phi\ln A)$ (Doi & Edwards 1989; this is based on an isotropic orientation distribution, which for a random centre of mass maximizes the

probability of such an interaction occurring). Thus, the error introduced into the mean fibre sedimentation speed by neglecting lubrication interactions is $O(\phi \ln A)$, which is 1 for the suspensions we consider.

Equations (2.2), (2.3), and (2.4), model interactions among N fibres in an unbounded suspension. In order to model an infinite suspension, we use periodicity to replicate the N fibres in a unit cell throughout space. To determine the field disturbances created at any point in space due to a periodic distribution of Stokeslets we use the periodic solution of the Stokes flow equations, $H_P(\boldsymbol{x})$, developed by Hasimoto (1959). This introduces a pressure gradient that opposes the flow created by the Stokeslets. This procedure renders the summation of divergent and conditionally convergent singularities well behaved. It has been used in Stokesian Dynamics simulations and is discussed in detail by Brady *et al.* (1988), Claeys & Brady (1993*a–c*), and references therein. Making use of $H_P(\boldsymbol{x})$, the periodically extended version of (2.2) becomes

$$\boldsymbol{U}_j + \boldsymbol{\Omega}_j \times s\boldsymbol{p}_j = \boldsymbol{v}^{\infty}(\boldsymbol{x}_{cj} + s\boldsymbol{p}_j) + \sum_{\substack{i=1 \\ i \neq j}}^{N} \int \boldsymbol{H}_P(\boldsymbol{x}_{c_i} + s'\boldsymbol{p}_i - \boldsymbol{x}_{c_j} - s\boldsymbol{p}_j) \cdot \boldsymbol{F}_i(s')\, \mathrm{d}s'$$

$$+ \int [\boldsymbol{H}_P((s-s')\boldsymbol{p}_j) - H((s-s')\boldsymbol{p}_j)] \cdot \boldsymbol{F}_j(s')\, \mathrm{d}s' + 2\left(\ln 2A + \ln \frac{(1-s^2)^{1/2}}{\hat{b}(s)}\right)(\boldsymbol{\delta} + \boldsymbol{p}_j\boldsymbol{p}_j) \cdot \boldsymbol{F}_j(s)$$

$$+ (\boldsymbol{\delta} - 3\boldsymbol{p}_j\boldsymbol{p}_j) \cdot \boldsymbol{F}_j(s) + (\boldsymbol{d} + \boldsymbol{p}_j\boldsymbol{p}_j) \cdot \int \frac{\boldsymbol{F}_j(s) - \boldsymbol{F}_j(s')}{|s-s'|}\, \mathrm{d}s', \quad j = 1, \ldots, N. \tag{2.5}$$

Equations (2.3), (2.4), and (2.5), can be solved to find the velocity, angular velocity, and Stokeslet distribution of each fibre in the periodically extended suspension. Our formulation is conceptually similar to the Stokesian dynamics simulations that have been used by Claeys & Brady (1993*a–c*) to simulate suspensions of spheroids. In both formulations, all particle interactions are related through a mobility tensor. The main difference is that we represent our fibers as line distributions of singularities, as opposed to multipoles at the centre of the body, essentially retaining all terms in the multipole expansion along the fibre axis. We do not include lubrication interactions. Additionally, we do not need to know the Faxén's law relationships for the body shapes. Our formulation is therefore very suitable for studying large-aspect-ratio bodies at concentrations up through semidilute, but less suitable for bodies of moderate aspect ratio or suspensions where lubrication interactions are important (Mackaplow & Shaqfeh 1996).

In order to solve the governing equations, we first discretize the integrals using Gauss–Legendre quadrature. Physical system parameters (fibre shape, aspect ratio, orientation distribution, and volume fraction) and the unit cell parameters (shape and number of fibres) are specified and used to generate random, non-overlapping fibre positions and orientations. The algorithm to do this, as well as tests to verify that the proper orientation distributions are generated, are discussed in detail by Mackaplow & Shaqfeh (1996). This reduces the discretized versions of equations (2.3), (2.4), and (2.5) to a set of $N \times (3M + 5)$ linear equations and unknowns. The unknowns for each fibre are three components of $\boldsymbol{F}(s)$ at each of the M discretization points, three components of $\boldsymbol{U}$, and two components of $\boldsymbol{\Omega}$ (there are only two linearly independent components of angular velocity because the slender-body theory approximation neglects variations in the velocity along fibre cross-sections). The system of equations is solved by an LUD (Lower Upper Diagonal) matrix decomposition algorithm. A typical simulation with $M = 13$ and 100 spheroidal inclusions in a cubic unit cell required about 5 minutes of

CPU time on a CRAY C90 supercomputer. For each set of physical parameters, the equations were solved for 10–20 different particle configurations and the results were ensemble averaged.

The present formulation cannot be used to directly simulate suspensions of cylindrical fibres, the fibre shape most commonly used in experimental studies. This is because the slender-body theory approximation is not valid near the ends of cylinders, resulting in a numerical instability that propagates throughout the entire solution vector. Mackaplow *et al.* (1994) studied the mathematically analogous problem of determining the thermal conductivity of a suspension of highly conducting fibres. By retaining higher-order terms in the slender-body theory approximation and neglecting the $O(b)$ regions at the end of the fibres they were able to get numerically convergent solutions for both spheroidal and cylindrical fibres. Although body shape had a quantitative effect on the results, they found that for both body shapes the effect of interfibre interactions was qualitatively similar and mainly a function of nl^3. The simulations of fibre sedimentation we present in this section all used spheroidal fibres, since this shape does not give rise to numerical difficulties. However, based on the above, we believe the results are relevant to systems of cylindrical fibres providing nl^3 and fibre aspect ratio are held constant.

The goal of our simulations is to determine the properties of disordered suspensions. Although the fibres in each unit cell are disordered, the system is ordered on the length scale of the unit cell. Since the behaviour of each fibre will be most greatly influenced by the fibres closest to it, the larger the periodic box, for a given suspension concentration, the better we expect our model to approximate the behaviour of a true disordered system. For our studies of the thermal conductivity (Mackaplow *et al.* 1994), and rheology (Mackaplow & Shaqfeh 1996) of fibre suspensions, we were always able to make our unit cells sufficiently large that the properties of the suspension were independent of cell size. However, for given suspension concentrations, similar cell sizes did not yield cell-size-independent sedimentation velocities and angular speeds. Since the computational effort per simulation, for a given suspension concentration, $\sim$ (box size)^9 (because the number of particles/box, N, $\sim$ (box size)^3, and the number of calculations for the matrix inversion $\sim N^3$) computing limitations prevented us from making our unit cells much larger.

The reason for this difficulty was discussed by Phillips, Brady & Bossis (1988). They showed that the finite box size effects on the suspension viscosity are at most $O(N^{-1})$, thus decaying rapidly with cell size. In contrast, the effect on sedimentation speed is $O(N^{-1/3})$, and thus decays very slowly. In Appendix A, based on the work of Phillips *et al.* (1988) and Ladd (1990), we develop an analytic finite box size effect correction for the velocity of isotropic fibres sedimenting in cubic unit cells

$$\boldsymbol{U} = \left[\mathbf{11} + \mathbf{22} + \left(1 - \frac{(\eta_o/\eta)(4am/3)(l/h) \times (1 + O(l/h))}{(\ln 2A + C_2 + O(1/\ln 2A))p_3 p_3 + \ln 2A + C_1 + O(1/\ln 2A)} \right)^{-1} \mathbf{33} \right] \cdot \boldsymbol{U}(N). \quad (2.6)$$

$\boldsymbol{U}(N)$ and $\boldsymbol{U}$ are the particle velocity as measured in an N-particle unit cell and the velocity if the same particle resided in a disordered suspension, respectively; C_1 and C_2 are $O(1)$ constants that are functions of body shape (see equation (1.4)); h is the unit cell length; η/η_o is the ratio of the suspension viscosity to that of the pure fluid, which may be determined using the results of Mackaplow & Shaqfeh (1995); and a is a constant that depends on the unit cell lattice. We have assumed that $\boldsymbol{g} = |\boldsymbol{g}|\mathbf{3}$ and $\mathbf{1}$ and $\mathbf{2}$ are orthogonal unit vectors in the directional perpendicular to gravity. Equation (2.6)

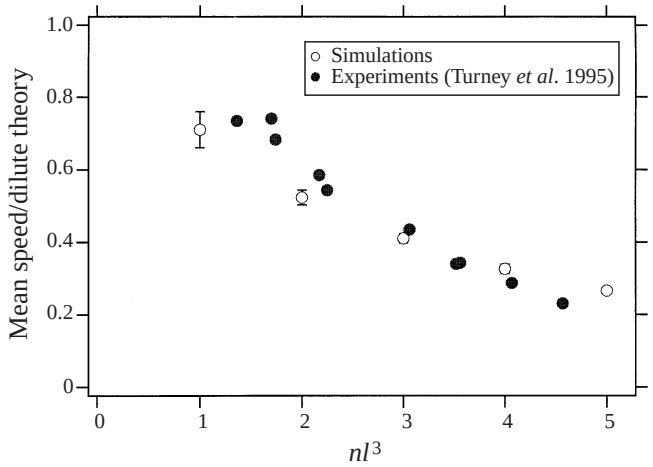

FIGURE 1. Mean sedimentation speed of an isotropic suspension of particles. Numerical simulations (spheroids, aspect ratio = 15.6) and the experimental results of Turney *et al.* (1995) (cylinders, aspect ratio = 17 ± 4) are plotted as a function of nl^3.

makes use of a two-term asymptotic expansion for the mobility of a periodic array of fibres that is developed in Appendix B. As discussed by Phillips *et al.* (1988) and in Appendix A, the finite box size effects on the rotational mobility decay as $(l/h)^3$, which is much more rapid than the decay of the translational mobility effects. However, because of the elongated nature of the fibres and the computational limits on the number of fibres that can be simulated, except at very dilute concentrations, $h/l \sim O(1)$. Thus it is of interest as to how to shape the unit cell to minimize such effects. In Appendix A we show that this can be done by using a unit cell that is elongated in the direction of the preferred fibre orientation.

2.2. *Results and discussion*

We used 100 spheroidal fibres/unit cell in all of the following Monte Carlo simulations. Unless otherwise stated, the fibre orientation distribution was isotropic and the cell was cubic. Individual fibre sedimentation velocities were corrected for finite box size effects using equation (2.6). For the first set of simulations we will present, the suspension viscosity required for the correction was obtained from the numerical results of Mackaplow & Shaqfeh (1996); for the last set, it was estimated using the dilute theory corrected for two-body interactions, presented by the same authors, which they found to be very accurate over the concentration range we consider. Mean sedimentation speeds are compared to those in dilute, isotropic suspensions, which, using equation (1.4), can be shown to be

$$\langle \boldsymbol{U} \rangle_{Isotropic}^{Dilute} = \frac{V_p g \Delta\rho}{8\pi\eta_0 l}[(4\ln 2A + 3C_1 + C_2)/3]\hat{\boldsymbol{g}}. \tag{2.7}$$

A dilute theory that takes into account two-body interactions, which is developed in Appendix C,

$$\langle \boldsymbol{U} \rangle_{Isotropic}^{2\text{-}body} = \langle \boldsymbol{U} \rangle_{Isotropic}^{Dilute} - \frac{V_p g \Delta\rho}{8\pi\eta_0 l}[1.509 nl^3/\ln 2A]\hat{\boldsymbol{g}} \tag{2.8}$$

is also presented.

In figure 1 we have compared our simulations of the mean sedimentation speed of

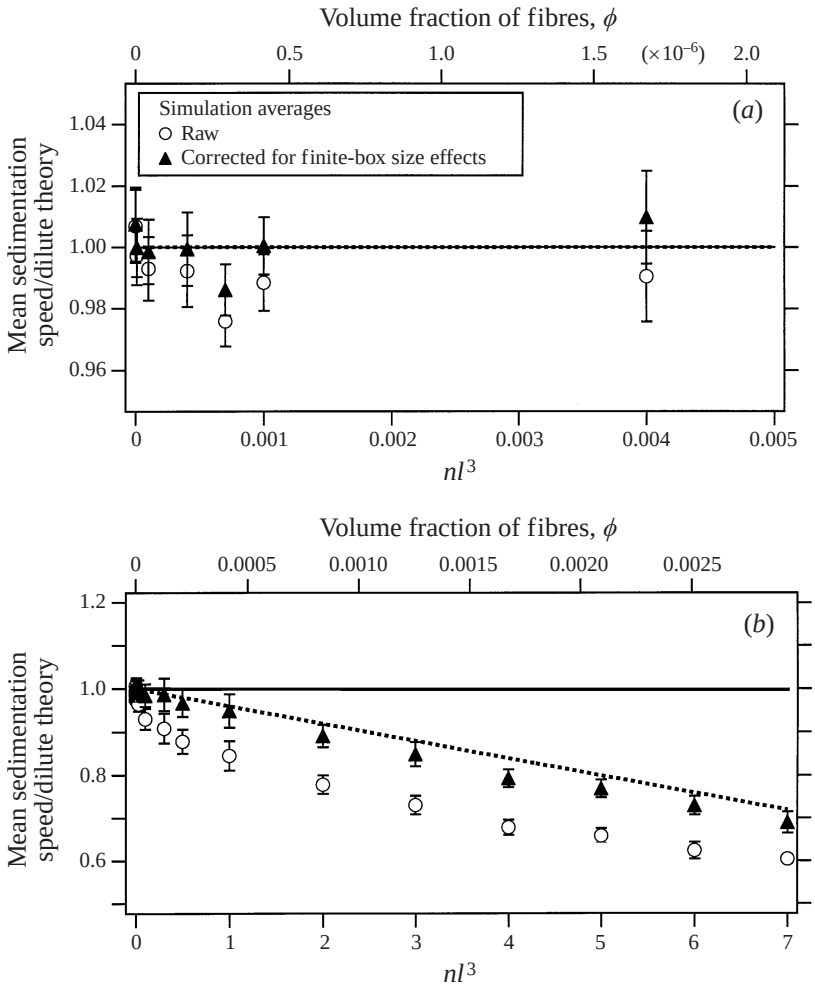

FIGURE 2. Mean sedimentation speed of an isotropic suspension of prolate spheroids with an aspect ratio of 100 as a function of concentration. Shown are the dilute theory (solid line), the dilute theory with two-body interactions (dotted line), and simulated results (both with and without corrections for finite box size effects, equation (A 11)). The error bars are 95% confidence intervals. (*a*) Dilute concentrations; (*b*) non-dilute concentrations.

a suspension of fibres with an aspect ratio of 15.6 to the experimental results of Turney *et al.* (1995). Since the experimental investigators used cylindrical fibres, the two sets of data are compared for common values of nl^3, not ϕ. This is based on the dilute theory corrected for two-body interactions, equation (2.8), which shows that nl^3 is the concentration parameter that determines interactions. The agreement between experiments and simulations is qualitatively and quantitatively quite good. Both show the mean sedimentation speed decreasing with increasing suspension concentration. The reduction, relative to the dilute theory, ranges from $\approx 30\%$ at $nl^3 = 1$ to $\approx 75\%$ at $nl^3 = 5$. However, as mentioned previously, these experiments assume that (i) the mean sedimentation speed in the suspension is equal to that of the upper suspension/fluid interface, and (ii) the suspension remains homogeneous and isotropic for the duration of the experiment. Turney *et al.* (1995) have not tested these assumptions. Additionally, for most of the data presented, $nl^3 > A/(2\pi)$ and $\phi^{1/2} \not< O(1)$.

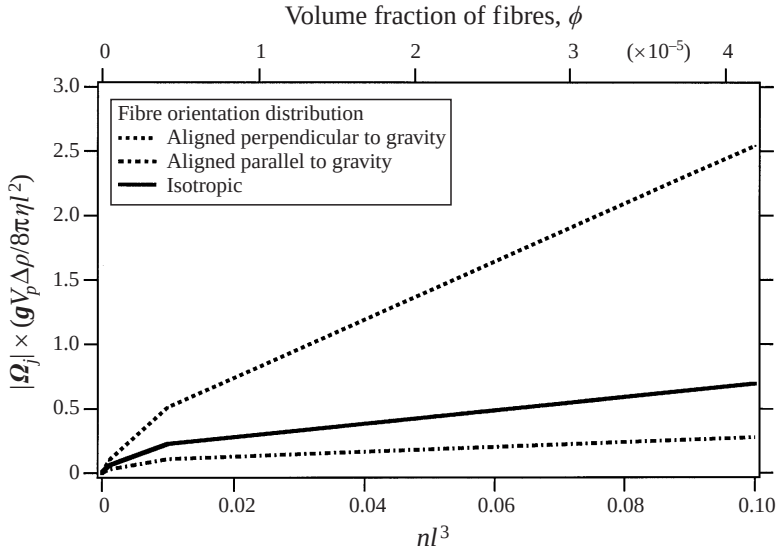

FIGURE 3. Mean angular speed of suspensions of prolate spheroids with an aspect ratio of 100 as a function of orientation distribution and concentration.

At such concentration the slender-body theory approximation underestimates the effect of fibre interactions (Mackaplow & Shaqfeh 1996, §2.1). Thus, the particularly good quantitative agreement between the simulations and experiments must be considered somewhat fortuitous. Nonetheless, we believe that figure 1 shows that our simulations are capturing the important physics in sedimenting suspensions.

Figure 2 shows the simulated mean sedimentation speed of a suspension of fibres with an aspect ratio of 100 as a function of concentration. Part (*a*) demonstrates that simulation results not corrected for finite box size effects show a systematic negative deviation from the dilute theory, even for suspension concentrations of $nl^3 \quad O(1)$. The data presented in part (*b*) suggest that the uncorrected, non-dimensionalized sedimentation speeds $\sim 1 - O(nl^3)^w$, where $w < 1$. Both these observations are consistent with the predicted finite box size effects discussed in §2.1 and Appendix A. The results corrected for finite box size effects presented in figure 2 show the mean sedimentation speed of the suspension decreasing approximately linearly with concentration up to at least $nl^3 = 7$, the highest concentration simulated. The results are in excellent quantitative agreement with the dilute theory that corrects for two-body interactions, equation (2.8), even for $nl^3 > 1$, where we expect multibody interactions to be important. A similar result has been found in studies of fibre suspension thermal conductivity (Mackaplow *et al.* 1994) and rheological behaviour (Mackaplow & Shaqfeh 1996).

Figure 3 shows the mean fibre angular speed in a sedimenting suspension of fibres with an aspect ratio of 100 as a function of concentration and orientation distribution. We have considered isotropic distributions and those aligned both parallel and perpendicular to gravity. For aligned suspensions, the unit cells were dilated by a factor of 6 in the direction of fibre alignment. This was done to minimize finite box size effects on fibre rotation, as suggested by the analysis of Appendix A. We have only shown data for $nl^3 \leqslant 0.1$, since for these dilute suspensions the periodic boxes will be largest, and thus the finite box size effects smallest. Figure 3 shows that the average fibre

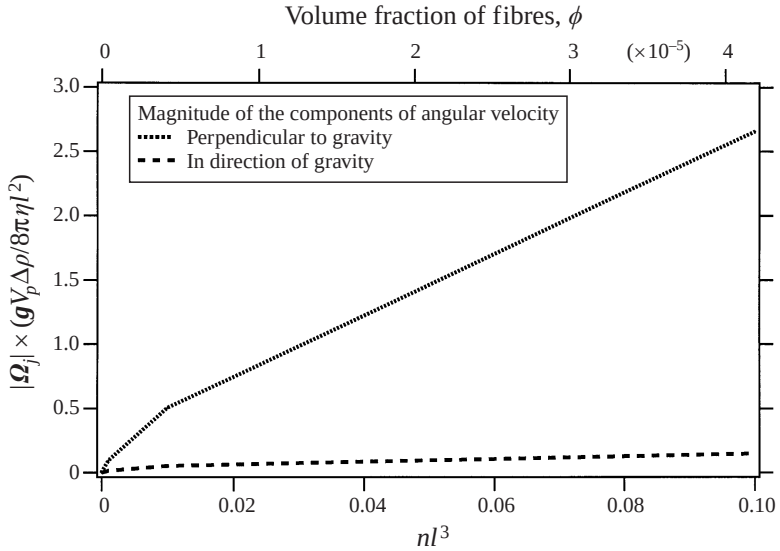

FIGURE 4. The mean magnitude of the components of the particle angular velocity vector perpendicular to and in the plane of gravity, as a function of concentration. The suspension consists of prolate spheroids with an aspect ratio of 100 aligned perpendicular to gravity.

angular speed is largest in suspensions where all fibres are aligned perpendicular to gravity and smallest in ones where the fibres are aligned parallel to gravity. The results for fibres aligned perpendicular to gravity are further analysed in figure 4, where we have divided the rotations into the magnitudes of the angular velocities perpendicular and parallel to gravity. If the rotations were purely random, these two components would be equal. However, we see instead that the rotation of the fibres is composed nearly entirely of angular velocities perpendicular to gravity, thus causing the fibres to become more aligned with the gravitational vector. The combined results shown in figures 3 and 4 suggest that the orientation distribution in a dilute sedimenting suspension of fibres will evolve to favour particles aligned in the direction of gravity. Such behaviour is seen in the dynamic point particle simulations discussed in §3 and the experimental studies referenced therein.

3. Dynamic simulations of sedimentation

3.1. *Introduction*

In the simulations described in the preceding section, we assumed particular fibre spatial and orientational distributions. However, as discussed in the Introduction, these quantities will evolve in time and presumably reach steady-state values, which are independent of the initial condition. Thus, we wish to perform dynamic simulations to see how the particle spatial and orientation distributions evolve. As discussed by Mackaplow (1995), integrating the Monte Carlo simulations forward in time is computationally prohibitive. Additionally, since the finite box size affects particle rotations (Appendix A) these effects may also cause inaccuracies in the suspension evolution as a model for an unbound settling suspension.

A simplified method to study the dynamics of a sedimenting suspension is to approximate the disturbance created by any fibre as that of a point force in the

direction of gravity. In such 'point particle' simulations, the effect of a fibre on the translation, $\boldsymbol{U}_i'$, and rotation, $\mathrm{d}\boldsymbol{p}_i'/\mathrm{d}t$, of another fibre are given by

$$\boldsymbol{U}_i' = \left(\frac{\boldsymbol{x}\boldsymbol{x}}{|\boldsymbol{x}|^3} + \frac{\boldsymbol{\delta}}{|\boldsymbol{x}|}\right)\cdot \boldsymbol{F}, \tag{3.1}$$

$$\frac{\mathrm{d}\boldsymbol{p}_i'}{\mathrm{d}t} = \boldsymbol{\Omega}(\boldsymbol{x})\cdot\boldsymbol{p}_i + \lambda''(\boldsymbol{\delta} - \boldsymbol{p}_i\boldsymbol{p}_i)\cdot\boldsymbol{E}(\boldsymbol{x})\cdot\boldsymbol{p}_i, \tag{3.2}$$

where

$$\lambda'' \equiv (r_e^2 - 1)/(r_e^2 + 1), \tag{3.3}$$

$$\boldsymbol{\Omega}(\boldsymbol{x}) \equiv \tfrac{1}{2}[(\nabla \boldsymbol{H}[\boldsymbol{x}]\cdot\boldsymbol{F}) + (\nabla\boldsymbol{H}[\boldsymbol{x}]\cdot\boldsymbol{F})^T], \tag{3.4}$$

$$\boldsymbol{E}(\boldsymbol{x}) \equiv \tfrac{1}{2}[(\nabla \boldsymbol{H}[\boldsymbol{x}]\cdot\boldsymbol{F}) - (\nabla\boldsymbol{H}[\boldsymbol{x}]\cdot\boldsymbol{F})^T]; \tag{3.5}$$

$\boldsymbol{x}$ is the vector between fibre positions and r_e is the effective fibre aspect ratio, which is in turn related to the rotation rate of a fibre in a linear flow field (Bretherton 1962; Anczurowski & Mason 1968). The latter is equal to the true aspect ratio, A, for spheroids and $1.29A/(\ln A)^{1/2}$ for cylinders (Cox 1970). The benefits of using point particle simulations are: (i) They only require $O(N^2)$ evaluations of $S_P(\boldsymbol{x})$ per time step, which is more than 100 times fewer than the number required for the Monte Carlo simulations. (ii) There is no longer a coupling between the fibre force distributions and their velocities and angular velocities. Thus instead of having to solve a coupled set of integral equations at each time step, we have the computationally less intensive task of integrating a coupled set of ordinary differential equations forward in time. (iii) As shown in Appendix A, since rotational finite box size effects will only be due to particle dipoles and higher-order multipoles, they will not affect these simulations. The details of the simulation algorithm and the range of particle concentration over which they may be good approximations to fibre suspensions are discussed below.

3.2. *Mathematical formulation of the problem*

If we assume $\boldsymbol{g} = |\boldsymbol{g}|\mathbf{3}$, then the non-dimensionalized ordinary differential equations governing the velocity and rotation of sedimenting point particles are

$$\frac{\mathrm{d}\boldsymbol{R}_j}{\mathrm{d}t} = [\lambda\boldsymbol{p}_j\boldsymbol{p}_j + \lambda'(\boldsymbol{\delta} - \boldsymbol{p}_j\boldsymbol{p}_j) + 2\boldsymbol{\delta}(c_{33} - c)]\cdot\mathbf{3} + \sum_{\substack{i=1\\ i\neq j}}^{N} \boldsymbol{H}_P[\boldsymbol{R}_j - \boldsymbol{R}_i]\cdot\mathbf{3}, \tag{3.6}$$

$$\frac{\mathrm{d}\boldsymbol{p}_j}{\mathrm{d}t} = \sum_{\substack{i=1\\ i\neq j}}^{N} [\boldsymbol{\Omega}_S[\boldsymbol{R}_j - \boldsymbol{R}_i]\cdot\boldsymbol{p}_j + \lambda''(\boldsymbol{\delta} - \boldsymbol{p}_j\boldsymbol{p}_j)\cdot\boldsymbol{E}_S[\boldsymbol{R}_j - \boldsymbol{R}_i]\cdot\boldsymbol{p}_j] \quad i = 1, \ldots, N, \tag{3.7}$$

where

$$\boldsymbol{\Omega}_S(\boldsymbol{x}) \equiv \tfrac{1}{2}[(\nabla\boldsymbol{H}_P(\boldsymbol{x})\cdot\mathbf{3}) + (\nabla\boldsymbol{H}_P(\boldsymbol{x})\cdot\mathbf{3})^T],$$

$$\boldsymbol{E}_S(\boldsymbol{x}) \equiv \tfrac{1}{2}[(\nabla\boldsymbol{H}_P(\boldsymbol{x})\cdot\mathbf{3}) - (\nabla\boldsymbol{H}_P(\boldsymbol{x})\cdot\mathbf{3})^T],$$

$$c_{33} - c = \tfrac{1}{2}\lim_{\boldsymbol{x}\to\mathbf{0}}[\boldsymbol{H}_P(\boldsymbol{x}) - \boldsymbol{H}(\boldsymbol{x})]:\mathbf{33}$$

and $\boldsymbol{R}_i$ is the coordinate of the centre of fibre i. $\nabla\boldsymbol{H}_P(\boldsymbol{x})\cdot\mathbf{3}$ was evaluated using an algorithm developed by Mackaplow (1995). Since point particles have no dipoles, they make no contribution to the suspension stress. Thus, $\eta = \eta_0$ in equation (2.6), which is used to correct each particle velocity at every time step.

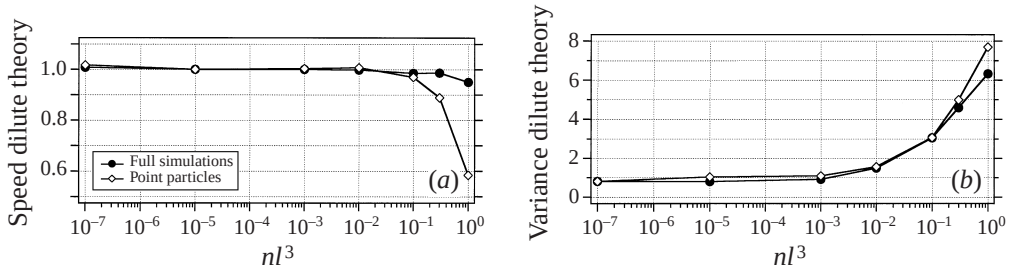

FIGURE 5. Comparison of the point particle and full Monte Carlo simulations for the sedimentation of an isotropic suspension of spheroids ($A = 100$) as a function of concentration. (*a*) Mean sedimentation speed, (*b*) velocity variance.

Point particle simulations neglect the effect of particle shape and aspect ratio on hydrodynamic interactions. However, the effect of these two parameters on the isolated fibre rotational and translational mobility tensors are fully retained. This is done by choosing values of λ, λ', and λ'', using equations (1.4) and (3.3), that correspond to the particles we wish to simulate.

In a real suspension, when two fibres approach each other to within a distance of $O(l)$, there will generally be some mutual enhancement of their sedimentation speeds. This will increase with decreasing separation distance and, in the limit of two fibres aligned and touching end to end, the enhancement approaches a factor of 2. Higher-order multipoles are important to accurately capture the effect of such interactions. In contrast, when two point particles approach within a distance l of each other, the effect of their mutual interactions will be to create aphysically large sedimentation velocities that diverge as $1/r$. To prevent this aphysical behaviour in our simulations, when calculating interactions between particles separated by distances $< l$ we normalize the length of the interparticle separation vector to be l. This is admittedly a somewhat arbitrary choice, motivated by the fact that higher-order multipole interactions should become important when the interparticle separation distance is $O(l)$. Additionally, the 'cut off' distance for the interactions must not be less than approximately $l/\ln 2A$, since below such separations distances the point interactions predict more than a doubling of the sedimentation speed of the two interacting fibres. Nonetheless, as discussed below, at the concentrations we simulate, the majority of the fibres do not initially have other fibres within a distance of l and this algorithm is shown to be reasonable approximation to the full Monte Carlo simulations.

By considering only leading-order hydrodynamic interactions in our point particle simulations, an error of $O(h/l)$, or equivalently, $O(nl^3)^{1/3}$, in introduced. To get a more quantitative estimate of this error, figure 5 compares the sedimentation behaviour predicted by the point particle simulations at particular initial particle configurations to that predicted by the Monte Carlo simulations. 100 bodies per cubic unit cell were used, so the unit cell sizes ranged from $1000l$ to $4.6l$. All results were corrected for finite box size effects. We see that the mean sedimentation speed and velocity variance predicted by the point particle simulations agree with the results of the more accurate Monte Carlo simulations to within 3 % for suspension concentrations up to $nl^3 = 0.1$.

In figure 6 we have plotted the mean fibre angular speed from the point particle simulations at a suspension concentration of $nl^3 = 0.1$. It is approximately independent of box size. This supports our conclusion that fibre angular velocities are not affected by finite box size effects in these simulations.

Dynamic simulations were performed by integrating equations (3.6), modified using

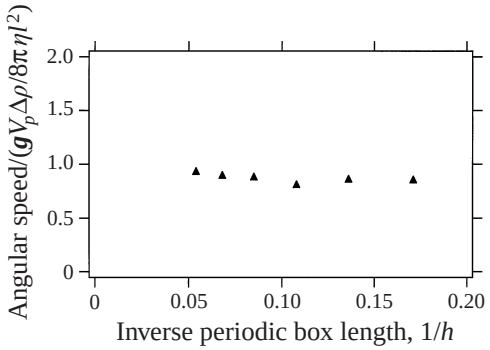

FIGURE 6. Mean angular speed predicted by point particle simulations as a function of periodic box size.

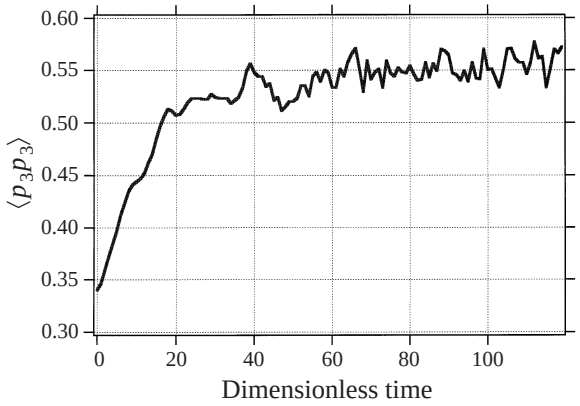

FIGURE 7. Simulated $\langle p_3 p_3 \rangle$ as a function of time in a sedimenting fibre suspension. Initially isotropic suspension of prolate spheroids: $A = 100$, $nl^3 = 0.1$.

equation (2.6) to correct for finite size effects, and (3.7) forward in time using a Runge–Kutta algorithm. 100 particles were allowed to sediment for 120 'Stokes times', where one Stokes time is defined as the time it would take a non-interacting, isotropic suspension to sediment one fibre half-length, based on the mean suspension velocity. When, during the course of a simulation, a particle left the periodic box, it was replaced by its particular periodic extension that enters the box at the same instant.

3.3. *Results and discussion*

The following simulations all used 100 particles in cubic unit cells. The fibres were initially homogeneously distributed and isotropically oriented. For each suspension concentration examined, simulations were performed for 10 different initial configurations. After verifying that each of the configurations evolved in the same qualitative way, the results were averaged.

3.3.1. *Prolate spheroids: aspect ratio* $= 100$; $nl^3 = 0.1$

We first simulated a suspension of prolate spheroids with an aspect ratio of 100 at a concentration of $nl^3 = 0.1$. Figure 7 shows the mean second moment of the orientation vector in the direction of gravity, $\langle p_3 p_3 \rangle$, as a function of time. As the

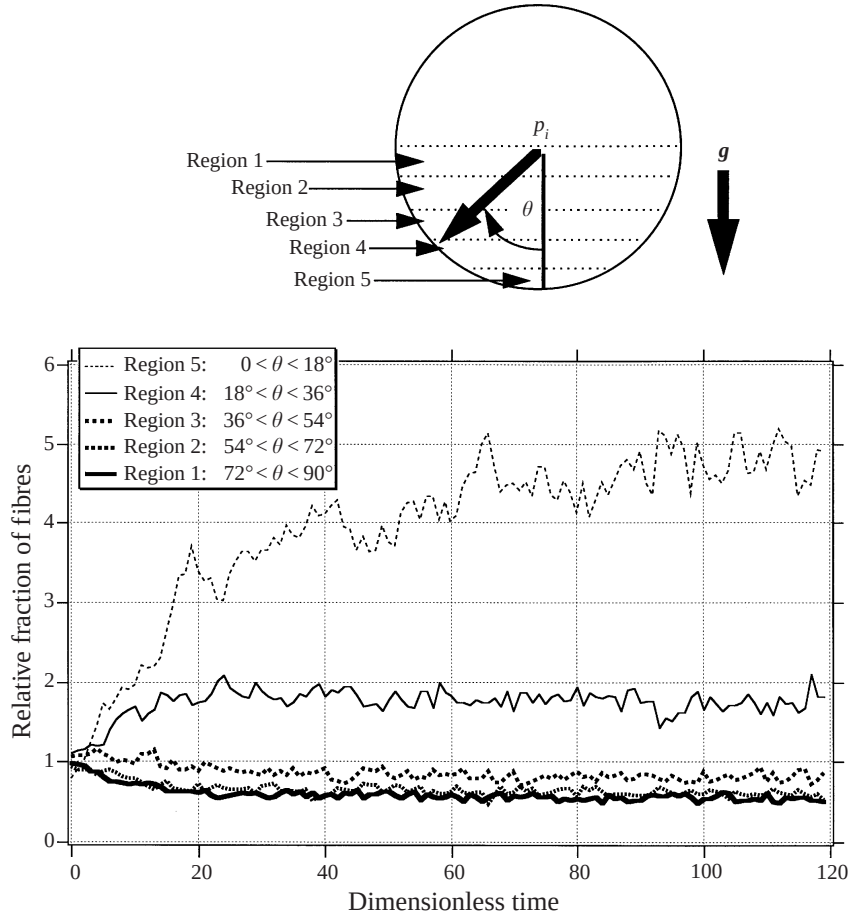

FIGURE 8. Transient histogram of fibre orientation distribution in a sedimenting fibre suspension. Frequencies are normalized relative to that in an isotropic distribution. θ is the angle relative to gravity. Initially isotropic suspension of prolate spheroids: $A = 100$, $nl^3 = 0.1$.

suspension sediments, $\langle p_3 p_3 \rangle$ increases from the isotropic value, 1/3, and after about 60 Stokes times, reaches a steady-state value of approximately 0.55. The seemingly random variation with time about the steady state value after this can be attributed to the fact that our system contains a finite number of particles and that the individual particles undergo flipping motions, as will be discussed in §3.3.2.

To better quantify the orientation distribution, figure 8 shows the time evolution of a histogram of fibre orientations. The bins of the histogram are five equal-sized ranges of the angle with respect to gravity. The bin values are normalized by the number of fibres that would be in each if the suspension were isotropic ($100 \times (\cos(\theta_1) - \cos(\theta_2))$, where θ_1 and θ_2 are the ranges of the histogram bin and $\theta_1 < \theta_2$). As with $\langle p_3 p_3 \rangle$, the distribution reaches a steady state after approximately 60 Stokes times. At steady state, the number of fibres in region five, the region containing fibres most aligned with gravity, has increased by a factor of four to five over that in an isotropic distribution. This corresponds to 20% to 25% of all fibre orientations being in this range. The number of fibres in region four, the second most aligned region, increased by about a factor of two. The other three regions show a depletion of fibres. These results are consistent with the results in figure 7.

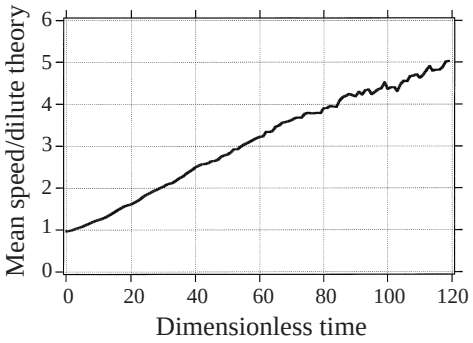

FIGURE 9. Mean sedimentation speed as a function of time. Initially isotropic suspension of prolate spheroids: $A = 100$, $nl^3 = 0.1$.

Figure 9 shows the mean sedimentation speed in the suspension, relative to that in a non-interacting isotropic suspension, as a function of time. The speed increases linearly with time, starting at about one and reaching approximately five after 120 Stokes times (a few simulations were run for 200 Stokes times and showed a continued linear increase of the mean speed with time). Even if all fibres in the sedimenting suspension aligned with gravity, but were otherwise homogeneously distributed in space, this could only account for an increase in the mean sedimentation speed by a factor of about 1.4. Thus, most of the increase must be due to the development of spatial inhomogeneities. This inference is supported by figure 10, where we have displayed the transient mean fibre closest approach distance. This is calculated by sequentially choosing each fibre in the unit cell as the 'test fibre', and for each test fibre determining the smallest of the centre-to-centre distances between it and all of the other fibres in the unit cell and all adjacent ones. These distances are then arithmetically averaged. In figure 10 we see that the mean fibre centre closest approach distance decreases by nearly a factor of two, from $1.2l$ to $0.7l$, throughout the course of the simulations. This suggests that particle clustering is leading to the increased sedimentation speed.

To study the development of the fibre spatial configuration in more detail, we have shown the evolution of the three-dimensional, two-point centre-of-mass distribution function in figure 11. By definition, if a fibre is centred at the origin of the coordinate system shown, this function tells us the probability of another fibre being at any other position. Because of the periodicity of our system, we have limited the size of our domain to approximately one periodic box (the periodic box is a cube with sides of $10l$). The function is normalized such that for a homogeneous distribution it will be unity everywhere. To facilitate data interpretation, regions where the function is less than unity have been rendered transparent.

Initially, within our accuracy of mapping the three-dimensional distribution, the suspension is homogeneous. As the suspension sediments, the fibres cluster into long streamers in the direction of gravity. This structure is quite evident after about 50 Stokes times. Throughout the course of the simulation, the structure becomes more defined and the density within the streamer, particularly at the origin, continues to increase. The occurrence of anisotropic particle clustering, with gravity being the preferred direction, was predicted by Koch & Shaqfeh (1989). It causes both the particles and fluid to be rapidly convected downward in regions of high particle density.

The monotonic decay of the distribution away from the origin in figure 11 shows that

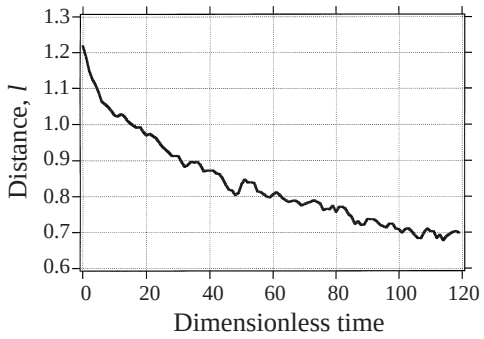

FIGURE 10. Mean fibre centre closest approach distance in a sedimenting suspension as a function of time. Initially isotropic suspension of prolate spheroids: $A = 100$, $nl^3 = 0.1$.

a single streamer forms. This suggests that the size of the periodic box is choosing the length scale of the inhomogeneities, $l_{inhomog}$. Under such conditions, one would expect that our simulated results would underestimate the time it would take to form streamers in unbounded suspensions, and therefore the rate of increase in the mean suspension speed would also be smaller for unbounded systems. Additionally, the simulated inhomogeneity in the gravitational direction is longer than the size of the periodic box. Thus, the interactions of these streamers across boxes in the vertical direction also artificially increases the sedimentation speed. These effects could have been reduced by choosing a rectangular unit cell that was shorter in the direction of gravity than the other two directions. Unfortunately, this would have had the detrimental aphysical effect of causing the dense regions in periodic boxes to begin overlapping in the direction of gravity more rapidly. In contrast, elongating the unit cell in the direction of gravity would have reduced the latter effect, but exacerbated the problem of the periodic box choosing the interstreamer length scale, i.e. forcing an even smaller length scale onto the system.

Recall that Koch & Shaqfeh (1989) predicted that $l_{inhomog} \sim O(nl)^{-1/2}$. For our simulations $(nl)^{-1/2} = 3l$. Since the $10l$ box seems to be choosing the length scale of the inhomogeneity, this suggests that the theory underpredicts the interstreamer spacing. However, since $10l$ and $3l$ are the same order, to better evaluate the accuracy of the Koch & Shaqfeh (1989) theory to predict $l_{imhomog}$ we would need to use a much larger unit cell. Unfortunately, since the number of particles required per unit cell, and thus the required computational effort, increases as N^3, this is not computationally feasible.

Since particle clustering is occurring, we need to examine how well the point particle approximation will capture the effect of particle interactions throughout the course of the simulation. During the simulation, the average closest approach distance between fibre centres, l_{clapp}, decreases by nearly a factor of two. By noting that $l_{clapp} \sim (nl^3)^{1/3}$, we see that this is equivalent to the local concentration in the vicinity of a fibre increasing to approximately $nl^3 = 0.8$. Figure 5 shows that at such concentrations point particle simulations overestimate the effect of interactions on particle mobilities. However, even though it is possible that the quantitative accuracy of the simulations decreases as they progress in time, this does not invalidate our basic findings that hydrodynamic interactions result in preferred fibre alignment in the direction of gravity, streamer formation, and increased sedimentation speeds.

As a check to see if the finite box size corrections were producing the observed fibre clustering, simulations were also executed in which no such corrections were made to fibre velocities. This did not affect the development of the suspension structure.

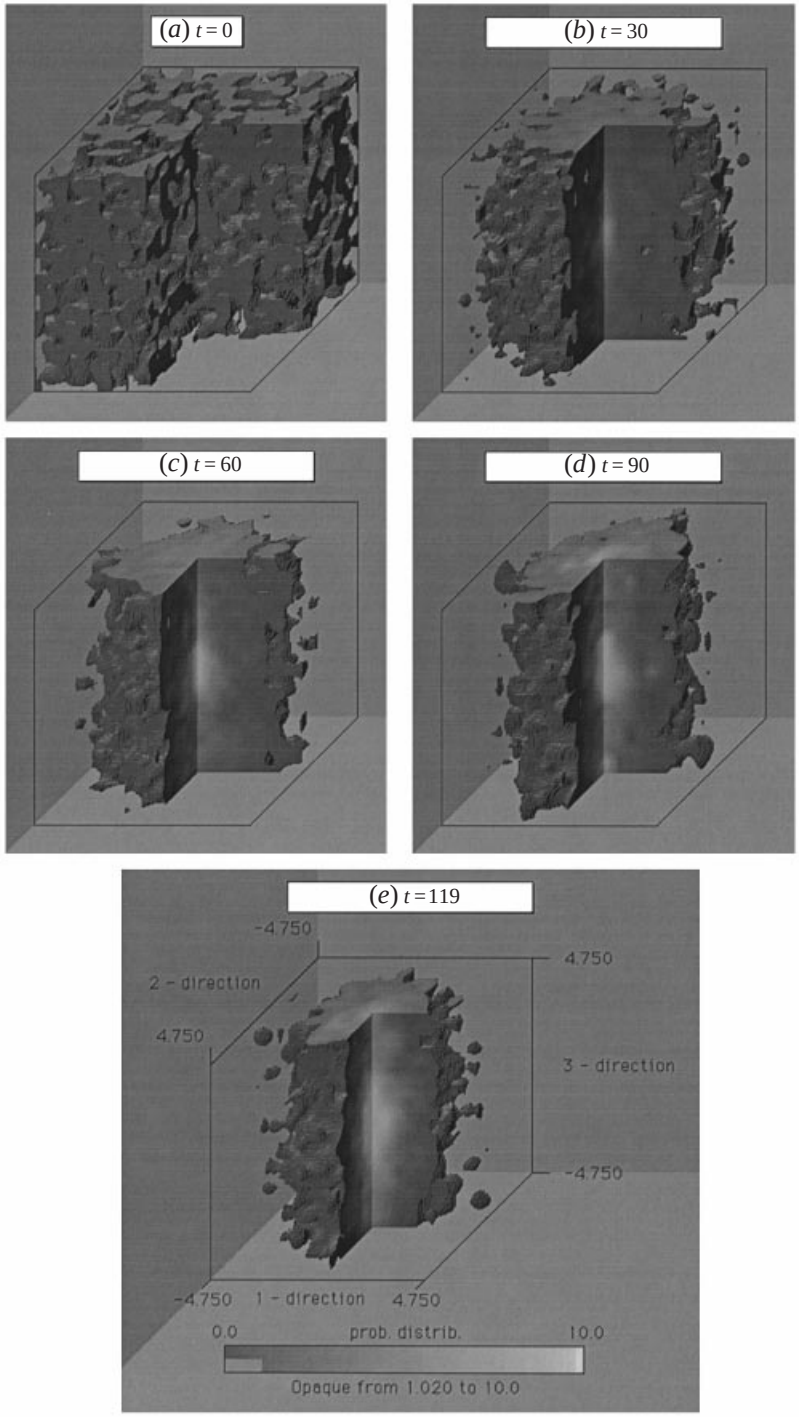

FIGURE 11. Time evolution of the three-dimensional, two-point fibre centre of mass distribution function in a sedimenting suspension. For a homogeneous distribution, it will be unity everywhere. Values less than unity are rendered transparent; values greater than 10 are treated as 10. Initially isotropic suspension of prolate spheroids: $A = 100$, $nl^3 = 0.1$. Time is in units of Stokes times.

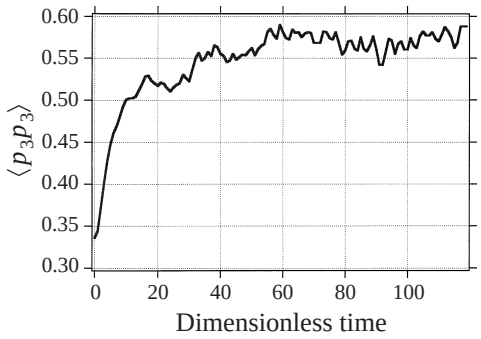

FIGURE 12. Simulated $\langle p_3 p_3 \rangle$ as a function of time in a sedimenting suspension. Initially isotropic suspension of slender cylinders; $A = 9.4$, $nl^3 = 0.061$.

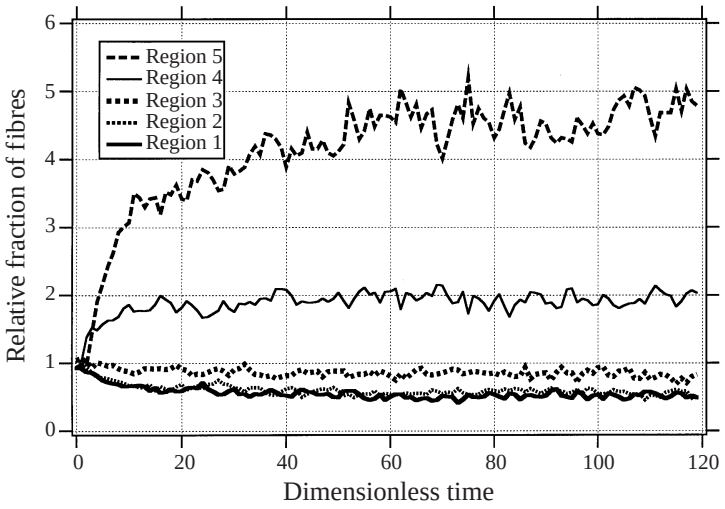

FIGURE 13. Transient histogram of fibre orientation distribution in a sedimenting suspension. Frequencies are normalized relative to that in an isotropic distribution. θ is the angle relative to gravity. Initially isotropic suspension of slender cylinders; $A = 9.4$, $nl^3 = 0.061$. Regions defined in figure 8.

3.3.2. *Slender cylinders: aspect ratio* $= 9.4$; $nl^3 = 0.061$

In order to study how sensitive the simulation results are to the system parameters, we repeated them using suspensions of slender cylinders having aspect ratios of 9.4 at a concentration of $nl^3 = 0.061$. Figures 12–15 show the time evolution of $\langle p_3 p_3 \rangle$, the orientation distribution histogram, the mean sedimentation speed, and the average fibre centre closest approach distance, respectively. The results are nearly identical to those in §3.3.1. The only exceptions are that the rate of increase in the mean sedimentation speed is about 20% slower and the mean particle closest approach distance is larger. This is due to the suspension concentration being more dilute, so it takes longer for particle clustering to occur. The results from these two sets of simulations suggest that the evolution of the particle positional and orientational configurations in a sedimenting suspension of fibres is relatively insensitive to the details of the body shape and aspect ratio.

Herzhaft *et al.* (1996) experimentally tracked the position and orientation of individual glass fibres (aspect ratio $= 10.6 \pm 2.5$) in a dilute ($nl^3 = 0.09 \pm 0.03$) sedimenting suspension. Due to vigorous agitation, the initial orientation distribution

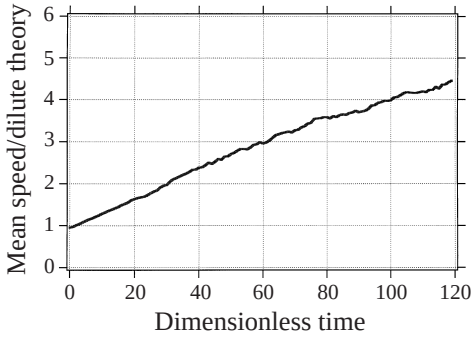

FIGURE 14. Mean sedimentation speed as a function of time in a sedimenting suspension. Initially isotropic suspension of prolate spheroids: $A = 9.4$, $nl^3 = 0.061$.

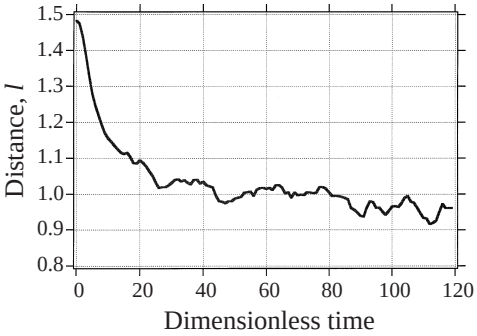

FIGURE 15. Mean fibre centre closest approach distance as a function of time is a sedimenting suspension. Initially isotropic suspension of slender cylinders: $A = 9.4$, $nl^3 = 0.061$.

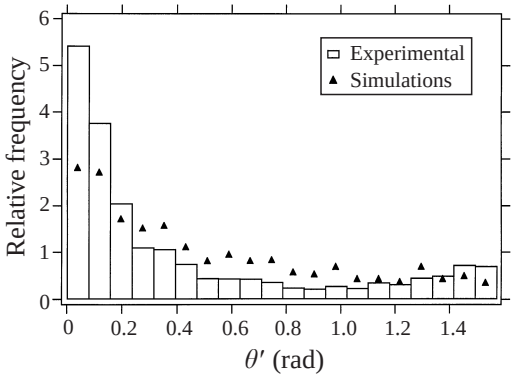

FIGURE 16. Fibre orientation distribution in a sedimenting suspension. θ' is the in-plane angle relative to gravity. Distributions are normalized relative to that in an isotropic suspension.

was assumed to be isotropic, and this was checked by examining the initial conditions in a few runs. In figure 16 we have compared the steady-state orientation distribution in a plane parallel to gravity to the predictions of our simulations. Both show the fibres preferentially oriented in the direction of gravity, although the degree of anisotropy is less in the simulations than in the experiments. The polydispersity of the experimental suspensions may be a factor in this quantitative discrepancy. Herzhaft *et al.* (1996) also showed that although the orientation distribution may reach a steady state, individual fibre orientations do not. Rather, a fibre spends most of the time in one of the two

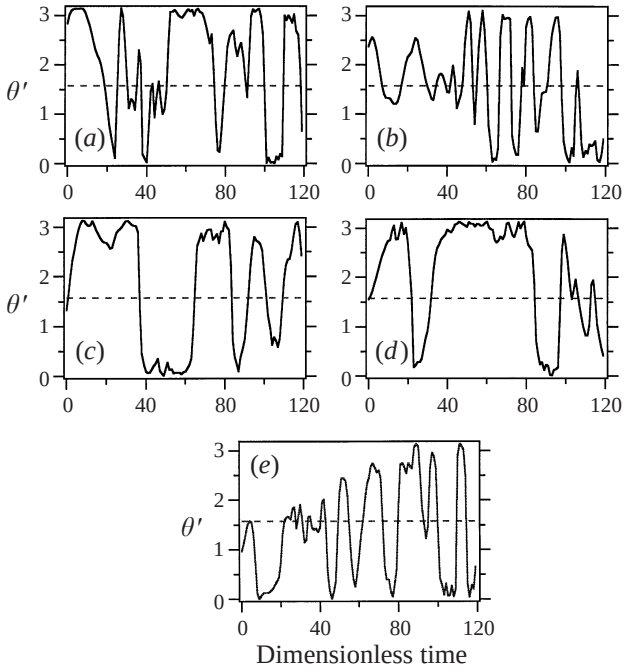

FIGURE 17. Transient numerical simulations of fibre orientations in a sedimenting suspension for five randomly selected fibres. θ' is the in-plane measured angle relative to gravity.

orientations aligned with gravity, while occasionally flipping between them. In figure 17 we plot the simulated, transient fibre orientation time for five randomly selected fibres. The rotation rates appear to be correlated with the instantaneous orientations. In particular, whereas fibres nearly always rapidly rotate through orientations perpendicular to gravity, they often linger in orientations nearly aligned with gravity. This is most evident in parts (*c*) and (*d*). This flipping motion is somewhat similar to fibres in a shear flow rotating in Jeffrey orbits. Indeed, the clustering of sedimenting fibres into vertical streamers leads to a shear flow on the length scales of the spatial inhomogeneities – and suggests that this is the mechanism that produces the flipping of fibres and thus the anisotropic orientation distribution. We also note that the time scale for flipping is much shorter in the simulations than in the experiments. The reason for this will be discussed shortly.

Also consistent with our simulations, Herzhaft *et al*. (1996) observed fibre clustering and an increase in the mean sedimentation speed beyond that which could be attributed to fibre alignment. However, unlike in our simulations, both eventually reached steady states that were less dramatic than seen in the simulations. We believe this discrepancy is because in our simulations: (i) the box size appears to choose an artificially small interstreamer spacing, thus allowing the fibre clusters to be larger and grow more rapidly, and (ii) we neglect solid body contacts, and thus the rotational and translational steric hindrances which will inhibit the continual densification of clusters. It is also possible that higher-order multipole interfibre hydrodynamic interactions may suppress further clustering as fibres become very close. As a result, the spatially periodic shear flow that develops along with the streamer formation will be stronger in the simulations than in the experiments. Thus, fibres flip more rapidly in the former than the latter. However, despite some quantitative discrepancies with the experimental

data, the key point is that the numerical simulation successfully predicted the steady-state fibre orientation distribution, fibre flipping, the development of spatial inhomogeneities, and substantial enhancement of the mean suspension sedimentation speed.

4. Conclusions

The understanding of the sedimentation behaviour of fibre suspensions under viscous flow conditions requires answering two important, coupled questions: (i) How does the orientation and spatial distribution of the particles evolve, and what steady-state distributions are achieved, and (ii) for a given spatial and orientation distribution, how do interparticle hydrodynamic interactions affect the sedimentation speed of the particles? By a slight decoupling of the two problems, we have been able to use two different types of numerical simulations to gain detailed qualitative and quantitative information about the sedimentation behaviour of fibre suspensions.

In §2, we focused on answering the latter of these questions – for a given distribution of fibres, what is the effect of hydrodynamic interactions on the sedimentation behaviour. Particular orientation and spatial distributions of the fibres were assumed. We then determined the effect of the hydrodynamic interactions between fibres using Monte Carlo simulations in which fibres were represented as line distributions of singularities. This problem formulation allowed us to study suspension concentrations up to and including those in the semidilute regime. For homogeneous suspensions with isotropic orientation distributions, we found that the effect of fibre interactions was to hinder the mean sedimentation speed in the suspension. This hindrance was a linear function of suspension concentration and was surprisingly well predicted by a dilute theory that only considered two-body interactions. Our numerical simulations showed excellent agreement with experimentally determined hindrance functions for non-dilute suspensions. However, the experimental study only tracked the fall of the sediment interface, did not measure the fibre orientation distribution, and operated at concentrations slightly above those where we expect our simulations to be able to fully capture the effect of interfibre interactions. Thus, although we believe the qualitative agreement suggests we are capturing the basic physics of the sedimenting system, the excellent quantitative agreement must be considered somewhat fortuitous.

In §3 we focused on answering the first of the two questions posed – how will the orientation and spatial distributions of fibres in a sedimenting suspension evolve? We did this by performing dynamic point particle simulations. The treatment of hydrodynamic interactions is less exact than in the Monte Carlo simulations, but still accurate for dilute suspensions. Our simulations predict that a dilute sedimenting suspension will achieve a steady-state orientation distribution that favours particle alignment in the direction of gravity. The distribution of fibres in the suspension becomes inhomogeneous, as fibres cluster into long streamers in the direction of gravity. This leads to a strong downward convection of fluid and particles in the streamers, thus producing enhanced mean particle sedimentation speeds. Such streamer formation was predicted theoretically by Koch & Shaqfeh (1989). These streamers drive a shear flow, on the length scale of the suspension inhomogeneities. This produces a flipping motion of the fibres (similar to the Jeffrey orbits of a fibre in a shear flow) where the preferred fibre orientation after the 'flips' is aligned with gravity. All of the above observations were in good agreement with the experimental data of Herzhaft *et al.* (1996). Our simulations results also show little sensitivity to the fibre shape and aspect ratio, within the limited range examined.

It has been observed that in suspensions containing particles of different mobilities, such as spheres of different sizes or densities, a similar type of streamer formation may occur at concentrations above a critical value, usually about 10% (Davis & Acrivos 1985). The denser or larger particles will gather into regions of large downward fluid convection and the smaller or lighter particles will collect in regions of fluid upwelling. The particles rapidly segregate into two separate regions at different heights, and thereafter sedimentation progresses with the two regions remaining homogeneous. Our dynamic simulations suggest that suspension polydispersity is not a necessary condition for such streamer formation to happen. It may also occur in a monodisperse suspension if particle mobility is a strong function of orientation. Unlike the case of polydisperse suspensions of spheres, the instability we examine occurs at very low concentrations, $nl^3 < O(1)$.

As noted previously, since many previous experimental studies of fibre sedimentation focused on measuring the fall of the sediment interface (Anselmet 1989; Kumar & Ramarao 1991; Turney *et al.* 1995), their relevance to understanding the mean sedimentation speed of fibres in suspension must be viewed with some skepticism. However, for $nl^3 \geqslant O(1)$, all of the studies found that at the steady state, the mean fall speeds were greatly hindered relative to the dilute theory. This suggests that regardless of whether particle clustering is occurring or not, at such concentrations the net effect of interparticle hydrodynamic interactions is to hinder the mean particle sedimentation speed. Further study of fibre suspensions at such concentrations is needed.

The authors would like to acknowledge support for this work from both a Presidential Young Investigator Award, Grant No. CTS-90557284, and a fellowship from the David and Lucile Packard Foundation, to E.S.G.S. as well as a Merck Fellowship to M.B.M. Computer resources (CRAY C-90) were supplied by the San Diego Supercomputer Center.

Appendix A. Effects due to the finite size of the periodic box

A.1. *Translational mobility effects: effect of box shape and analytic corrections*

A.1.1. *Effect of periodic box shape*

By considering how the velocity of a fibre is affected by its periodic extensions in adjacent unit cells, we can determine a cell shape that will minimize finite box size effects. To begin, the disturbance velocity created by a single fibre, equation (2.1), can be written as a multipole expansion about the centre of the fibre, x_i, which we choose to be the origin. (Note that in this Appendix all equations will be presented using indicial notation to simplify the results). The expansion becomes

$$u_i'(x_i') = A_{ij}(x_i')\,F_j + B_{ijk}(x_i')\,D_{jk} + C_{ijkl}(x_i')\,E_{jkl} + \cdots, \tag{A 1}$$

where

$$A_{ij} \equiv H_{ij}(x_i' - x_i)|_{x_i=0} = (\delta_{ij} + \hat{x}_i'\,\hat{x}_j')/r,$$

$$B_{ijk} \equiv \frac{\partial}{\partial x_k} H_{ij}(x_i' - x_i)|_{x_i=0} = (\delta_{ij}\,\hat{x}_k' - \delta_{ik}\,\hat{x}_j' - \delta_{jk}\,\hat{x}_i' + 3\hat{x}_i'\,\hat{x}_j'\,\hat{x}_k')/r^2,$$

$$\begin{aligned} C_{ijkl} \equiv \frac{\partial^2}{\partial x_k\,x_l} H_{ij}(x_i' - x_i)|_{x_i=0} &= (\delta_{ij}\,\delta_{kl} - \delta_{ik}\,\delta_{jl} - \delta_{jk}\,\delta_{il})/r^3 \\ &+ 3(\delta_{ij}\,\hat{x}_l'\,\hat{x}_k' - \delta_{ik}\,\hat{x}_j'\,\hat{x}_l' - \delta_{jk}\,\hat{x}_i'\,\hat{x}_l')/r^3 \\ &+ 3(\delta_{jl}\,\hat{x}_i'\,\hat{x}_j' + \delta_{il}\,\hat{x}_i'\,\hat{x}_k' + \delta_{jl}\,\hat{x}_j'\,\hat{x}_k')/r^3 - 15\hat{x}_i'\,\hat{x}_j'\,\hat{x}_k'\,x_l'/r^3, \end{aligned}$$

$$r \equiv |x_i|, \quad \hat{x}_i \equiv x_i/r,$$

$$F_i \equiv \int f_i(s)\,\mathrm{d}s, \quad D_{ij} \equiv p_i \int f_i(s)\,s\,\mathrm{d}s, \quad E_{ijk} \equiv p_i p_j \int f_k(s)\,s^2\,\mathrm{d}s.$$

If we assume that $g_i = g\delta_{i3}$, then

$$f_i(s) = g_1(s)\,\delta_{i1} + g_2(s)\,\delta_{i2} + (h(s) + g_3(s))\,\delta_{i3}, \tag{A 2}$$

where $h(s)$ depends only on the shape of the fibre and satisfies

$$\int h(s)\,\mathrm{d}s = 1, \tag{A 3}$$

The functions $g_1(s)$, $g_2(s)$, $g_3(s)$ depend on the hydrodynamic interactions the fibre experiences. They satisfy

$$\int g_1(s)\,\mathrm{d}s = \int g_2(s)\,\mathrm{d}s = \int g_3(s)\,\mathrm{d}s = 0 \tag{A 4}$$

and vanish in the limit of an infinitely dilute suspension.

Next, we consider the effect of an imposed flow field, $u_i'(x_i)$, on the velocity of a fibre, U_i'. To leading order in slender-body theory (i.e. neglecting terms of $O(\ln 2A)^{-1}$)

$$U_i' = u_i'(s=0) + \left.\frac{\partial^2 u_i'}{\partial x_j\,\partial x_k}\right|_{s=0} p_j p_k/3 + \ldots. \tag{A 5}$$

We can combine equation (A 1) and its derivatives with equation (A 5) to determine how the velocity of a fibre is affected by one of its periodic extensions, yielding

$$U_i' = (\delta_{ij} + \hat{x}_i'\,\hat{x}_i')\,F_j/r \times (1 + O(1/r^2)). \tag{A 6}$$

Because of the symmetry of a periodic system, we have neglected interactions that are odd functions of x_i. Additionally, the effect of the adverse pressure gradient necessary for renormalization can be neglected, since it just creates a uniform flow whose strength depends only on fibre concentration. Thus, it does not affect our comparison of how the velocity of a fibre will be affected by its periodic extensions relative to that in other unit cells with the same volume but different shapes.

Equation (A 6) implies that in the limit of $h \quad l$, where h is the characteristic cell size, finite box size effects can be minimized by making the cell twice as long in the direction of gravity than perpendicular to it. Unfortunately, it also shows that such effects decay very slowly, as $1/h$, with increasing cell size (Phillips *et al.* 1988). Thus, we proceed with developing analytic corrections for finite box size effects.

A.1.2. *Analytic corrections for finite box size effects on particle mobilities*

Spheres. In order to determine the scaling of the finite box size effects on the mobility of a sedimenting suspension of spheres, Phillips *et al.* (1988) proposed modelling the system as a lattice of volume fraction ϕ/N sedimenting superimposed on a random, sedimenting suspension of volume fraction $\phi(1-1/N)$. This yields the proper $N^{-1/3}$ scaling of the finite box size effects. It also suggests that they can be corrected for by subtracting out the hindrance caused by the lattice of volume fraction ϕ/N using analytic formulas for the mobility of sedimenting arrays (the mobility effect of the random component of the suspension having concentration $\phi(1-1/N)$, not ϕ, is generally much smaller and can be neglected). However, this model is an approximation since the suspension of volume fraction $\phi(1-1/N)$ is actually not random, but ordered

on the length scale of the unit cell. Ladd (1990), numerical simulating suspensions of spheres, showed that the above correction did not yield sedimentation velocities that were independent of box size. However, by a slight modification to this algorithm, he was able to achieve box-size-independent results:

$$\mu = \mu(N) + \left(\frac{\eta_0}{\eta}\right)\left(\frac{\mu}{\mu_0}\right)\mu_{corr}(N), \tag{A 7}$$

where μ is the true particle mobility, μ_0 the single particle mobility in infinite fluid, $\mu(N)$ the mobility measured in an N-particle periodic system, $\mu_{periodic}$ the mobility of a periodic array having the same cell size as the N-particle periodic system and $\mu_{corr}(N) \equiv \mu_0 - \mu_{periodic}$; η and η_0 are the suspension and pure fluid viscosities, respectively. His modification included adding of the viscosity and mobility ratios. The ratio of viscosities implies that the interactions between a fibre and its periodic extensions are dampened by the extra suspension stress that the other particles create; the ratio of mobilities implies that any mobility hindrances must be scaled relative to the true particle mobility, not that of an isolated particle. Based on the proven success of equation (A 7), our approach is to develop mathematical generalizations of it for fibre suspensions. Since a force on an isolated fibre may induce motion in directions other than that of the applied force, fibre mobility must be treated as a tensor. Additionally, a scalar viscosity cannot generally be used to relate the fluid stress and strain tensors. We examine three different physical systems, in order of increasing complexity.

Fibres: dilute suspensions ($nl^3 < O(1)$). In dilute suspensions, the $O(nl^3)$ effect of the particles on the suspension stress is, by definition, small. Thus, we neglect the η_0/η term in equation (A 7). Under such conditions, two possible generalizations of equation (A 7) to fibre suspensions are

$$\mu_{ij}^{(M)} = \mu(N)_{ij}^{(M)} + T[\mu_{ij}^{(M)}; \mu(N)_{corr,ij}^{(M)}; \mu_{0,ij}^{(M)}]_{ij}, \tag{A 8}$$

where $T[a_{ij}; b_{ij}; c_{ij}]_{ij}$ is a tensor formed by an element by element multiplication of a_{ij} and b_{ij}, followed by a subsequent element by element division of the resulting tensor by c_{ij}, and

$$\mu_{ij}^{(M)} = \mu(N)_{ij}^{(M)} + \mu_{0,ik}^{(M),-1}\mu_{kl}^{(M)}\mu(N)_{corr,lj}^{(M)}. \tag{A 9}$$

The superscript (M) designates a particular fibre. If we assume $\hat{g}_i = \delta_{i3}$, and make use of an expression for the mobility of a simple cubic periodic array of fibres developed in Appendix B, then equation (A 8) becomes

$$U_i = \Bigg[\delta_{i1}\delta_{j1} + \delta_{i2}\delta_{j2} + \left(1 - \frac{(4am/3)(l/h) \times (1 + O(l/h))}{(\ln 2A + C_2 + O(1/\ln 2A))p_3 p_3 + \ln 2A + C_1 + O(1/\ln 2A)}\right)^{-1}\delta_{i3}\delta_{j3}\Bigg] U_j(N), \tag{A 10}$$

where $a \equiv 1.7601$ (simple cubic lattice), h is the size of the periodic box, $m \equiv (\frac{4}{3}\pi)^{1/3}$, C_1, C_2 are related to fibre shape (equation (1.4)) and $U_i(N)$ and U_i are the measured and true particle velocities, respectively. As a test of the validity of any proposed finite box size correction, 'correcting' the mobility of a sedimenting fibre lattice for finite box size effects should yield the mobility of an isolated fibre. This is the case for equation (A 10), but not for a similar correction developed using equation (A 9). Therefore, we will proceed using (A 10).

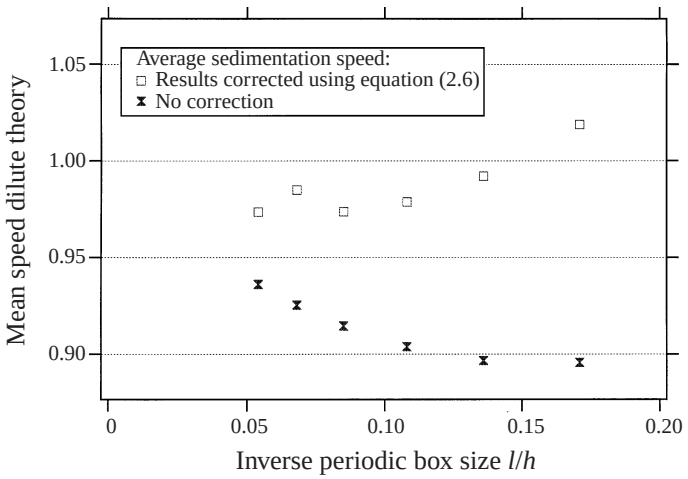

FIGURE 18. Mean sedimentation speed of a suspension, $nl^3 = 0.1$, of prolate spheroids with an aspect ratio of 100 as a function of inverse periodic box size. The suspension is isotropic and the periodic boxes are cubic. Each data point is an average of 10 simulations. Shown are simulation results that are uncorrected for finite box size effects and those corrected using equation (2.6). The dilute theory corrected for two-body interactions, equations (2.8), predicts a value of 0.99.

In figure 18 we have plotted the mean simulated fibre sedimentation speed in a dilute suspension, both corrected for finite box size effects using equation (A 10) and uncorrected, as a function of cell size. (Varying the latter over a sufficiently large range required using nearly 1000 particles/periodic box. This could only be done using the less computationally intensive 'point particle' algorithm. However, at the dilute concentration considered, $nl^3 = 0.1$, these are an excellent approximation to the full simulations (figure 5).) It shows that simulation results uncorrected for finite box size effects monotonically increase with increasing cell size. In contrast, results corrected by equation (A 10) show no consistent variation with box size for periodic box sizes $> 10l$. The fact that this converged value, 0.98 ± 0.01, is approximately the same as that predicted by the dilute theory corrected for two-body interactions (equation (2.8)), 0.99, suggests that for such box sizes equation (A 10) accurately corrects for finite box size effects.

Fibres: non-dilute, isotropic suspensions. In non-dilute suspensions, we may not neglect the effect of the fibres on the suspension stress. However, for the special case of isotropic fibre orientation distributions, it may be characterized by a scalar effective viscosity. If we assume that this enhanced viscosity serves to screen finite box size effects in the same way it does in a suspension of spheres (equation (A 7)), then equation (A 10) becomes

$$U_i = \left[\delta_{i1}\delta_{j1} + \delta_{i2}\delta_{j2} + \left(1 - \frac{(\eta_0/\eta)(4am/3)(l/h) \times (1 + O(l/h))}{(\lambda - \lambda')p_3 p_3 + \lambda'}\right)^{-1} \delta_{i1}\delta_{j3}\right] U_j(N). \tag{A 11}$$

Since, by definition, a point particle has no dipole, it makes no contribution to the suspension stress. Therefore, we cannot test this proposed correction using our point particle simulations.

Fibres: Non-dilute, anisotropic suspensions. In a non-dilute, anisotropic suspension, stress and strain are not related by a scalar viscosity, but rather by a fourth order

tensor. Under such conditions, it is not clear how the term (η_0/η) in equation (A 7) should be treated. Although we will not consider this case here, one possible approach, which reduces to equation (A 11) for isotropic suspensions, is shown in detail by Mackaplow (1995).

A.2. *Rotational mobility effects: effect of box shape*

We now wish to estimate what periodic box shapes will minimize finite box size effects on fibre rotation. To leading order in slender-body theory, the rotation rate of a fibre can be related to the imposed flow field by

$$\frac{\mathrm{d}p_i}{\mathrm{d}t} = \epsilon_{ijk}\,\omega_j\,p_k = \frac{3}{2}\int u_i'(sp_i)\,s\,\mathrm{d}s. \tag{A 12}$$

Using an analysis similar to that performed in §A.1, we can show that

$$\mathrm{d}p_i/\mathrm{d}t = (M_{ijkl}+N_{ijkl}+O_{ijkl})\,D_{kl}\,p_j/r^3\times(1+O(1/r^2)), \tag{A 13}$$

where

$$\begin{aligned} M_{ijkl} &= \delta_{ik}\,\delta_{jl}-\delta_{ij}\,\delta_{kl}-\delta_{jk}\,\delta_{il},\\ N_{ijkl} &= 3(\delta_{ik}\,\hat{x}_l\,\hat{x}_j-\delta_{ij}\,\hat{x}_k\,\hat{x}_l-\delta_{jk}\,\hat{x}_i\,\hat{x}_l+\delta_{jl}\,\hat{x}_i\,\hat{x}_k+\delta_{kl}\,\hat{x}_i\,\hat{x}_j-\delta_{il}\,\hat{x}_k\,\hat{x}_l),\\ O_{ijkl} &= -15\hat{x}_i\,\hat{x}_j\,\hat{x}_k\,\hat{x}_l, \quad D_{ij} = p_i\,b_j; \end{aligned}$$

b_j depends on the particular interactions a fibre experiences and, on average, has no preferred directions. Equations (A 13) implies that in the limit of (characteristic box size) $\gg$ l, for a given periodic box volume, finite box size effects can be minimized by elongating the periodic box in the direction of preferred fibre alignment. The $1/r^3$ decay of the interactions (Phillips *et al.* 1988) suggests that finite box effects will rapidly decrease with increasing box size. This is important, as we know of no theoretical way to correct for these effects.

Appendix B. Mobility of a periodic array of fibres

The translational mobility tensor of any periodic array may be written as

$$\boldsymbol{\mu} = \boldsymbol{\mu}_o-\Delta\boldsymbol{\mu}, \tag{B 1}$$

where $\boldsymbol{\mu}_o$ is the mobility of an isolated particle, and $\Delta\boldsymbol{\mu}$ is the hindrance due to the interactions with all of the other particles in the array. The latter is a function of lattice type, size, and particle orientation. By analogy, for a given gravitational body force, we may write

$$\boldsymbol{U} = \boldsymbol{U}_o-\Delta\boldsymbol{U}, \tag{B 2}$$

where $\boldsymbol{U}$ is the particle translational velocity.

Let us consider two physical systems: (*a*) a periodic array of spheres with radius l, and (*b*) a periodic array of fibres with half-length l, with identical lattice sizes and structures. The spheres and fibres have uniform, identical densities. By definition

$$\Delta\boldsymbol{U}_{sphere} = \rho V_{sphere}\,\Delta\boldsymbol{\mu}_{sphere}\cdot\boldsymbol{g}, \tag{B 3}$$

$$\Delta\boldsymbol{U}_{fibre} = \rho V_{fibre}\,\Delta\boldsymbol{\mu}_{fibre}\cdot\boldsymbol{g}, \tag{B 4}$$

where V_{sphere} and V_{fibre} are the volume of an individual sphere and fibre, respectively. In the limit of $h \gg l$, as seen from equation (A 6), the effect of any sedimenting particle on the velocity of another body is independent of particle shape. It depends only on

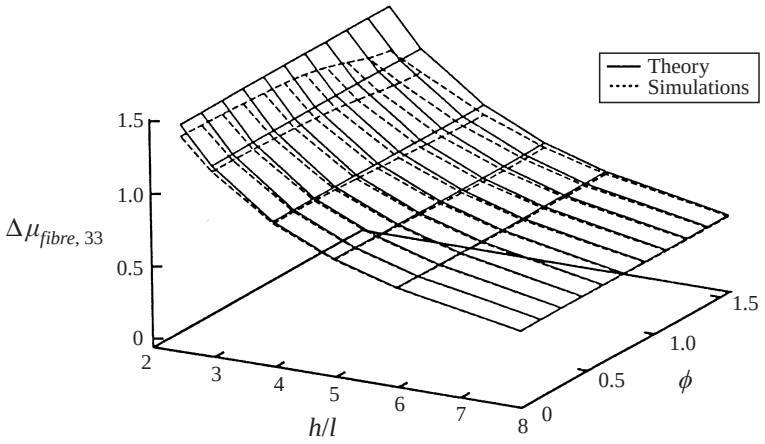

FIGURE 19. Comparison of theoretical prediction of $\Delta\mu_{fibre,33}$, from equation (B 8), to numerical simulations.

the total body force, $\boldsymbol{F}$, the particle exerts on the fluid. Likewise, the adverse pressure gradient introduced via renormalization also is proportional to the net force the particle exerts on the fluid. Thus, $\Delta\boldsymbol{\mu}_{sphere}$ and $\Delta\boldsymbol{\mu}_{fibre}$ are related by

$$\Delta\boldsymbol{\mu}_{fibre} = (V_{fibre}/V_{sphere})\,\Delta\boldsymbol{\mu}_{sphere} \times (1 + O(l/h)). \tag{B 5}$$

Combining equations (B 3), (B 4), and (B 5) yields

$$\Delta\boldsymbol{\mu}_{fibre} = \Delta\boldsymbol{\mu}_{sphere} \times (1 + O(l/h)). \tag{B 6}$$

Hasimoto (1959) determined $\Delta\boldsymbol{\mu}_{sphere}$ for SC, FCC, and BCC arrays of spheres

$$\Delta\boldsymbol{\mu}_{sphere} = \frac{1}{6\pi\eta_0 l}(a\phi_s^{1/3} - \phi_s - O(\phi_s^2))\boldsymbol{\delta}, \tag{B 7}$$

where ϕ_s is the volume fraction of spheres and a equals 1.760, 1.791, and 1.791 for SC, BCC, and FCC lattices, respectively. Equation (B 6) allows us to apply equation (B 7) to determining $\boldsymbol{\mu}_{fibre}$. Combining equation (1.4), (B 1), (B 6), and (B 7) yields

$$\boldsymbol{\mu}_{fibre} = \frac{1}{8\pi\eta_0 l}[(\ln 2A + C_2 + O(1/\ln 2A))\,\boldsymbol{pp} + (\ln 2A + C_1 + O(1/\ln 2A))\,\boldsymbol{\delta}]$$

$$-\frac{1}{8\pi\eta_0 l}(4am(nl^3)^{1/2}\,\boldsymbol{\delta}/3) \times (1 + O(nl^3)^{1/3}), \tag{B 8}$$

where $m \equiv (4\pi/3)^{1/3}$ and the latter term is $\Delta\boldsymbol{\mu}_{fibre}$.

We test the accuracy of equation (B 8) by considering a sedimenting simple cubic array of spheroids having an aspect ratio of 100. The planes of the lattice lie along the Cartesian coordinate axes and gravity is in the **3**-direction. We compare theoretical predictions of $\Delta\boldsymbol{\mu}_{fibre}$ to numerical simulations using the algorithm described in §2 with one particle/periodic box. Since only lattices having a closest approach between particles b are considered, the simulations will be highly accurate. $\Delta\boldsymbol{\mu}_{fibre}$ depends on lattice size, h, fibre orientation relative to gravity, ϕ, and projected angle in the (1, 2)-plane, θ (θ is defined such that at $\theta = 0$, $p_1 = 0$ and at $\theta = \pi/2$, $p_2 = 0$). However, our simulations have shown that the variation with θ is much weaker than with h or ϕ. Thus, we average over the variation with θ, e.g. $\tilde{\boldsymbol{\mu}}(\phi, h) = (1/2\pi)\int \boldsymbol{\mu}(\phi, \theta, h)\,\mathrm{d}\theta$. For the

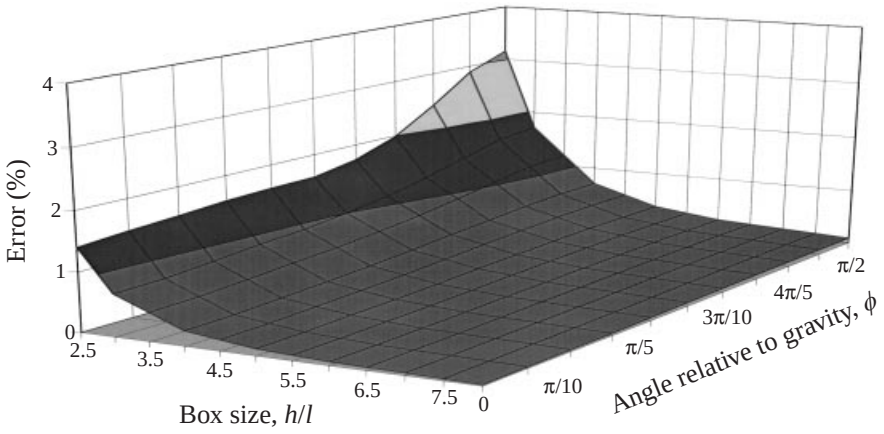

FIGURE 20. Error in theoretical prediction of $\Delta\mu_{fibre,33}$, equation (B 8). Values are non-dimensionalized by $\Delta\mu_{fibre,33}|_{nl^3=0}$.

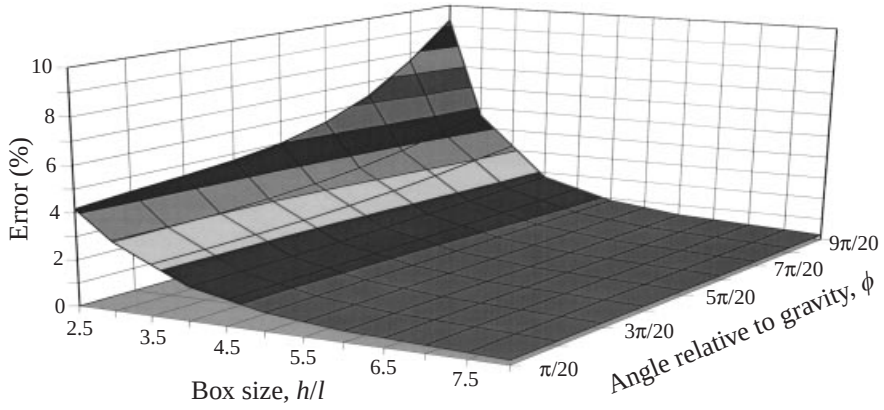

FIGURE 21. Error in theoretical prediction of $\Delta\mu_{fibre,13}$, equation (B 8). Values are non-dimensionalized by $\Delta\mu_{fibre,13}|_{nl^3=0}$.

following discussion, for notational simplicity, we will drop the ˜ notation from $\tilde{\boldsymbol{\mu}}$. All values are non-dimensionalized by $1/(8\pi\eta_0 l)$.

Figure 19 shows that the predictions of the sedimentation mobility hindrance, $\Delta\mu_{fibre,33}$, by equation (B 8) are in excellent agreement with the numerical simulations for h as small as $2.5l$. To get a more quantitative measure of the accuracy of the theory, in figure 20 we show the error in the theory normalized by the result for an isolated particle, e.g. $(\Delta\mu_{33,theory}-\Delta\mu_{33,simulation})/\mu_{fibre,33}|_{nl^3=0}$. The error introduced by using equation (B 8) is always less than 5%. Figure 21 shows a similar comparison for drift velocities, $\Delta\mu_{13,simulation}/\mu_{fibre,13}|_{nl^3=0}$ (note that $\Delta\mu_{13}$ and $\Delta\mu_{23}$ are related by the symmetry of the system, $\Delta\mu_{13}(\theta)=(\Delta\mu_{23}(\pi/2-\theta)$, so only one of them needs to be considered). For h as small $2.5l$, the maximum error in equation (B 8) is always less than 10%. In conclusion, by making use of the theoretical expression for the mobility of a periodic array of spheres (Hasimoto 1959), we have developed a two-term expansion for the mobility of cubic periodic arrays of fibres. Although the formula is developed for $h \gg l$, we show that it gives highly accurate results for cell sizes as small as $h \sim O(l)$.

Appendix C. The first effect of hydrodynamic interactions on the sedimentation velocity of a dilute, isotropic suspension of fibres

In this Appendix, we develop the correction term (including the first effects of hydrodynamic interactions) presented in (2.8) for the average sedimentation speed of a dilute, isotropic homogeneous suspension of sedimenting fibres. The calculation will make use of both the fact that the suspensions is dilute (so only terms up to $O(nl^3)$ will be retained, with $nl^3 \quad 1$) and that reflection interactions among fibres are 'weak' with each reflection being smaller by a factor of $1/\ln(2A)$ for $A \quad 1$. Thus terms up to $O(nl^3/\ln(2A))$ will be retained which represent the first non-zero average effect of two-particle interactions and comes from the so-called 'first reflection' interaction. We shall discuss this in detail below.

We begin by noting that the disturbance velocity created by a single slender fibre in an unbounded quiescent fluid under Stokes' flow conditions, can be written according to (2.1) as an integral of Stokeslets using slender-body theory, namely

$$\boldsymbol{v}^D(\boldsymbol{x}) = \int \boldsymbol{F}(s)\cdot\boldsymbol{H}(\boldsymbol{x}-\boldsymbol{x}_c-s\boldsymbol{p})\,\mathrm{d}s\times(1+O(b/h)), \tag{C 1}$$

where $\boldsymbol{v}^D$ is the disturbance velocity, $\boldsymbol{H}$ is the Oseen interaction tensor, and the remaining notation is described in §2.1. An approximation for the average disturbance velocity created by a fibre in a random, isotropic suspension of fibres can be written if we use the approximate averaged Green's function for the medium which was derived by Shaqfeh & Fredrickson (1990). Note that this Green's function does not include all multiparticle interactions but includes sums of infinite subclasses of these interactions as described in the appropriate reference (Shaqfeh & Fredrickson 1990) and referred to below. We then have

$$\boldsymbol{v}^D(\boldsymbol{x}) \approx \int \boldsymbol{F}(s)\cdot\boldsymbol{G}(\boldsymbol{x}-\boldsymbol{x}_c-s\boldsymbol{p})\,\mathrm{d}s, \tag{C 2}$$

where $\boldsymbol{G}$ is the Shaqfeh–Fredrickson Green's function for an isotropic suspension of slender fibres (Shaqfeh & Fredrickson 1990). The Fourier transform (indicated by the $\hat{}$) of this function is given by the expression (Shaqfeh & Fredrickson 1990)

$$\hat{\boldsymbol{G}} = \frac{\boldsymbol{\delta}-\boldsymbol{k}\boldsymbol{k}/k^2}{\mu k^2 - nQ(kl)}, \tag{C 3}$$

$$Q(kl) = \frac{\pi\mu l}{\ln(2A)}\left(\int_{-1}^{1}\mathrm{d}x([j_0^2(kxl)-1](1-x^2)+2[3j_1^2(kxl)+j_0^2(kxl)-1](1+x^2)\right), \tag{C 4}$$

where $\boldsymbol{k}$ is the wavenumber of the transform, $k=|\boldsymbol{k}|$, n is the number density of the fibres, j_0 and j_1 are the spherical Bessel functions of zero and first order respectively (Shaqfeh & Fredrickson 1990). Note that (C 2) includes the disturbance velocity created by the fibre whose centre is at $\boldsymbol{x}_c$ in the viscous fluid (i.e. that given by (C 1)) and also the disturbance velocities created by the other fibres as a result of the disturbance in (C 1). Thus it includes an approximation for the *reflected fields* which is the critical information necessary to calculate the correction to the sedimentation velocity. This approximation for the average reflected velocity disturbance can be written explicitly by subtracting (C 1) from (C 2) to yield

$$\boldsymbol{v}^{reflected}(\boldsymbol{x}) \approx \int \boldsymbol{F}(s)\cdot\Delta\boldsymbol{G}(\boldsymbol{x}-\boldsymbol{x}_c-s\boldsymbol{p})\,\mathrm{d}s, \tag{C 5}$$

where $\Delta \boldsymbol{G} = \boldsymbol{G} - \boldsymbol{H}$. The result given by (C 5) is not an exact result for the reflected field, but, it does contain the $O(1/\ln(2A))$ approximation for the average first reflection (cf. Shaqfeh & Fredrickson 1990). This is the information necessary to obtain the leading-order asymptotic correction to the sedimentation velocity.

Note that these reflected fields correct the sedimentation velocity in a simple way, since they act as an imposed solvent velocity on the fibre whose centre is at $\boldsymbol{x}_c$. Throughout the remaining development we shall let $\boldsymbol{x}_c = 0$ without loss of generality since the suspension is homogeneous. The correction to the sedimentation velocity for the fibre centred at the origin with orientation $\boldsymbol{p}$ engendered by these reflected disturbances is

$$\boldsymbol{U}' = \frac{1}{2l}\int_{-l}^{+l} \mathrm{d}s'\, \boldsymbol{v}^{reflected}(s'\boldsymbol{p}) = \frac{1}{2l}\int_{-l}^{+l} \mathrm{d}s' \int \mathrm{d}s\, \boldsymbol{F}(s)\cdot\Delta\boldsymbol{G}(s'\boldsymbol{p} - s\boldsymbol{p}). \tag{C 6}$$

Finally, if the orientations are isotropically distributed then to get the average change in the sedimentation velocity we need to average over the orientation $\boldsymbol{p}$ of the fibre at the origin. Thus we have

$$\langle \boldsymbol{U}' \rangle = \frac{1}{8\pi l}\int \mathrm{d}\boldsymbol{p} \int_{-l}^{+l} \mathrm{d}s'\, \boldsymbol{v}^{reflected}(s'\boldsymbol{p}) = \frac{1}{8\pi l}\int \mathrm{d}\boldsymbol{p} \int_{-l}^{+l} \mathrm{d}s' \int_{-1}^{+1} \mathrm{d}s\, \boldsymbol{F}(s)\cdot\Delta\boldsymbol{G}(s'\boldsymbol{p} - s\boldsymbol{p}), \tag{C 7}$$

where the orientation integral is over all orientations $\boldsymbol{p}$.

To this point we have developed an approximation but we have not explicitly used the facts that $nl^3 \quad$ and $1/\ln(2A) \quad 1$. To do this we first take $\boldsymbol{F}$ to be the leading-order force density in powers of $1/\ln(2A)$. We thus obtain

$$\boldsymbol{F} \approx \frac{\Delta\rho \boldsymbol{g} V_p}{2l}. \tag{C 8}$$

Expanding $\Delta\boldsymbol{G}$ in powers of nl^3 we obtain

$$\Delta\hat{\boldsymbol{G}} \approx \frac{nQ}{\mu^2 k^4}[\boldsymbol{\delta} - \boldsymbol{k}\boldsymbol{k}/k^2]. \tag{C 9}$$

We then define a function, $S(\boldsymbol{x})$, such that

$$\begin{aligned} S(\boldsymbol{x}) &= 1 \quad \text{if} \quad \boldsymbol{x} = s\boldsymbol{p}; \quad -l \leqslant s \leqslant l \\ &= \text{otherwise}, \end{aligned} \tag{C 10}$$

and note that

$$\hat{S} = 2l j_0(\boldsymbol{k}\cdot\boldsymbol{p}l). \tag{C 11}$$

Thus (C 7), using (C 8) and (C 10), can be rewritten

$$\langle \boldsymbol{U}' \rangle = \frac{\Delta\rho \boldsymbol{g} V_p}{16\pi l^2}\int \mathrm{d}\boldsymbol{p} \int \mathrm{d}\boldsymbol{x}' \int \mathrm{d}\boldsymbol{x}\, S(\boldsymbol{x}')\, S(\boldsymbol{x})\, \Delta\boldsymbol{G}(\boldsymbol{x}' - \boldsymbol{x}). \tag{C 12}$$

Using the convolution theorem and (C 9) we can rewrite the spatial integrals in terms of a single integral over the wavenumber $\boldsymbol{k}$

$$\langle \boldsymbol{U}' \rangle = \frac{\Delta\rho \boldsymbol{g} V_p}{4\pi l^2 (2\pi)^3}\int \mathrm{d}\boldsymbol{p} \int \mathrm{d}\boldsymbol{k} j_0^2(\boldsymbol{k}\cdot\boldsymbol{p}l)\frac{nQ}{\mu^2 k^4}[\boldsymbol{\delta} - \boldsymbol{k}\boldsymbol{k}/k^2]. \tag{C 13}$$

Finally, we can measure all angles in the space $\boldsymbol{p}$ with respect to the $\boldsymbol{k}$ and thus $\boldsymbol{k}\cdot\boldsymbol{p} = kx$. We can therefore integrate over the remaining angular coordinates which

are not x. Simplifying the remaining integrals after these angular integrations, non-dimensionalizing k with l, and substituting the definitions for $Q(kl)$, we obtain

$$\langle \boldsymbol{U}' \rangle = \frac{\Delta\rho \boldsymbol{g} V_p}{8\mu\pi l} \frac{nl^3 I}{\ln(2A)}, \tag{C 14}$$

where I is the integral defined

$$I = \frac{16}{3}\int_0^1 \mathrm{d}x \int_0^1 \mathrm{d}\xi \int_0^\infty \mathrm{d}k \frac{j_0^2(kx)}{k^2}([j_0^2(\xi k)-1](1-\xi^2)+2[3j_1^2(\xi k)+j_0^2(\xi k)-1](1+\xi^2)). \tag{C 15}$$

Numerically evaluating I we find $I \approx -1.509\ldots$ and with this result we have reproduced the two-body theory stated in (2.8).

As derived above, this correction includes the first reflection interactions from all second fibres approximated up to $O(1/\ln(2A))$. However, one may wonder whether this is in fact the leading-order correction to the sedimentation velocity from interparticle interactions. There are two other candidates which are not obviously higher order in either powers of nl^3 (as all three-body and multi-body interactions would be) or powers of $1/\ln(2A)$ (as all multiple reflections would be). These possibilities are direct interactions from a second body where the disturbance made by the second's sedimentation disturbs the velocity of our fibre at the origin and the related effect of the excluded volume of the fibre at the origin causing 'backflow' of solvent through the suspension. It is now well known that the 'direct' effects of a second fibre must sum to zero if the centre-of-mass probability of the second is uniform throughout space (this is one of the original renormalizations of Batchelor 1972). However, the centre-of-mass distribution (of the second particle) cannot be completely uniform throughout space because the fibre at the origin excludes volume. For the case of spheres this excluded volume causes a backflow through the suspension which creates the largest contribution to the leading-order hindrance of the sedimentation velocity (Batchelor 1972). In the sedimentation of fibres, however, the excluded volume for fibres which are isotropically oriented is $O(nl^2b)$ or $O(nl^3/A)$ (see for example, Doi & Edwards 1989) because of the fact that the fibres are very thin. Thus the correction due to excluded volume (and the backflow) is smaller by a factor of $\ln(A)/A$ and is negligible in the limit as $A \to \infty$.

REFERENCES

Anczurowski, E. & Mason, S. G. 1968 *Trans. Soc. Rheol.* **2**, 209.

Anselmet, M.-C. 1989 Contribution a l'etude des systemes fluide-particules: suspensions de cylindres, lits fluidses. PhD thesis, University of Provence, France.

Barnea, F. & Mizrahi, J. 1973 A generalized approach to the fluid dynamics of particulate systems: Part 1. General correlation for fluidization and sedimentation in solid multiparticle systems. *Chem. Engng J.* **5**, 171–189.

Batchelor, G. K. 1970 Slender-body theory for particles of arbitrary cross-section in Stokes flow. *J. Fluid Mech.* **44**, 419–440.

Batchelor, G. K. 1972 Sedimentation of a dilute suspension of spheres. *J. Fluid Mech.* **52**, 245–268.

Brady, J. F., Phillips, R. J., Lester, J. C. & Bossis, G. 1988 Dynamic simulation of hydrodynamically interacting suspensions. *J. Fluid Mech.* **195**, 257–280.

Bretherton, F. P. 1962 The motion of rigid particles in a shear flow at low Reynolds number. *J. Fluid Mech.* **14**, 284.

Claeys, I. L. & Brady, J. F. 1993*a* Suspensions of prolate spheroids in Stokes flow. Part 1. Dynamics of a finite number of particles in an unbounded fluid. *J. Fluid Mech.* **251**, 411–442.

Claeys, I. L. & Brady, J. F. 1993*b* Suspensions of prolate spheroids in Stokes flow. Part 2. Statistically homogeneous dispersions. *J. Fluid Mech.* **251**, 443–477.

Claeys, I. L. & Brady, J. F. 1993*c* Suspensions of prolate spheroids in Stokes flow. Part 3. Hydrodynamics transport properties in crystalline dispersions. *J. Fluid Mech.* **251**, 479–500.

Cox, R. G. 1970 The motion of long slender bodies in a viscous fluid. Part 2. Shear flow. *J. Fluid Mech.* **45**, 625–657.

Davis, R. H. & Acrivos, A. 1985 Sedimentation of noncolloidal particles at low Reynolds number. *Ann. Rev. Fluid Mech.* **17**, 91–118.

Davis, R. H. & Hassen, H. 1988 Spreading of the interface at the top of a slightly polydisperse sedimenting suspension. *J. Fluid Mech.* **196**, 107.

Doi, M. & Edwards, S. F. 1989 *The Theory of Polymer Dynamics*. Oxford University Press.

Ham, J. M. & Homsey, G. M. 1988 Hindered settling and hydrodynamic dispersion in quiescent sedimenting suspensions. *Intl J. Multiphase Flow* **14**, 533–546.

Happel, J. & Brenner, H. 1965 *Low Reynolds Number Hydrodynamics*. Prentice Hall.

Hasimoto, H. 1959 On the fundamental solutions of the Stokes equations and their application to viscous flow past a cubic array of spheres. *J. Fluid Mech.* **5**, 317–328.

Herzhaft, B., Guazelli, E., Mackaplow, M. B. & Shaqfeh, E. S. G. 1996 An experimental investigation of the sedimentation of a dilute fiber suspension. *Phys. Rev. Lett.* **77**, 290–293.

Koch, D. L. & Shaqfeh, E. S. G. 1989 The instability of a suspension of sedimenting spheroids. *J. Fluid Mech.* **209**, 521–542.

Kumar, P. & Ramarao, B. V. 1991 Enhancement of the sedimentation rates in fibrous suspensions. *Chem. Engng Commun.* **108**, 381–401.

Kuwabara, S. 1959 The forces experienced by randomly distributed parallel cylinders or spheres in a viscous flow at small Reynolds number. *J. Phys. Soc. Japan* **14**, 527–532.

Ladd, A. J. C. 1990 Hydrodynamic transport coefficients of random dispersions of hard spheres. *J. Chem. Phys.* **93**, 3484–3494.

Mackaplow, M. B. 1995 A study of the transport properties and sedimentation characteristics of fiber suspensions. PhD thesis, Stanford University.

Mackaplow, M. B. & Shaqfeh, E. S. G. 1996 A numerical study of the rheological properties of suspensions of rigid, non-Brownian fibres. *J. Fluid Mech.* **329**, 155–186.

Mackaplow, M. B., Shaqfeh, E. S. G. & Schiek, R. L. 1994 A numerical study of heat and mass transport in fibre suspensions. *Proc. R. Soc. Lond.* A **447**, 77–110.

Nicolai, H., Herzhaft, B., Hinch, E. J., Oger, L. & Guazzelli, E. 1995 Particle velocity fluctuations and hydrodynamic self-diffusion of sedimenting non-Brownian spheres. *Phys. Fluids* A **7**, 12–23.

Oberbeck, A. 1876 Ueber stationare flussigkeitbewegungen mit berucksicthigung der innernen reibung (on steady state fluid flow and the calculation of the drag). *J. Reine. Angew. Maths* **81**, 62–80.

Phillips, R. J., Brady, J. F. & Bossis, G. 1988 Hydrodynamic transport properties of hardsphere dispersion. I. Suspensions of freely mobile particles. *Phys. Fluids* **31**, 3462–3472.

Reinhart, W. H., Singh, A. & Werner, S. 1989 Red blood cell aggregation and sedimentation: the roll of cell shape. *Brit. J. Hematol.* **73**, 551–556.

Richardson, J. F. & Zaki, W. N. 1954 Sedimentation and fluidisation: Part 1. *Trans. Inst. Chem. Engrs* **32**, 35–53.

Russel, W. B., Saville, D. A. & Schowalter, W. R. 1991 *Colloidal Dispersions*. Cambridge University Press.

Shaqfeh, E. S. G. & Fredrickson, G. H. 1990 The hydrodynamic stress in a suspension of rods. *Phys. Fluids* A **2**, 7–24.

Turney, M. A., Cheung, M. K., McCarthy, M. J. & Powell, R. L. 1995 Hindered settling of rod-like particles measured with magnetic resonance imaging. *IAChE J.* **41**, 251–257.

Zuzovsky, M., Adler, P. M. & Brenner, H. 1983 Spatially periodic suspensions of convex particles in linear shear flows. iii. Dilute arrays of spheres suspended in Newtonian fluids. *Phys. Fluids* **26**, 1714–1723.